Impact of the recent measurement of $(g\text{-}2)_\mu$, the LHC search for supersymmetry, and the LZ experiment on the minimal supersymmetric standard model

Yangle He,[†] Lei Meng,[*] Yuanfang Yue,[‡] and Di Zhang[§]
School of Physics, Henan Normal University, Xinxiang 453007, China

(Received 9 May 2023; accepted 8 November 2023; published 11 December 2023)

Motivated by the recent measurement of muon anomalous magnetic moment at Fermilab, the rapid progress of the LHC search for supersymmetry, and the significantly improved sensitivities of dark matter direct detection experiments, we studied their impacts on the minimal supersymmetric standard model (MSSM). We conclude that higgsino mass should be larger than about 500 GeV for $M_1 < 0$ and 630 GeV for $M_1 > 100$ GeV, where M_1 denotes the bino mass. These improved bounds imply a tuning of $\mathcal{O}(1\%)$ to predict the Z-boson mass and simultaneously worsen the naturalness of the Z- and h-mediated resonant annihilations to achieve the measured dark matter density. We also conclude that the LHC restrictions have set lower bounds on the sparticle mass spectra: $m_{\tilde{\chi}_1^0} \gtrsim 210$ GeV, $m_{\tilde{\chi}_2^0}, m_{\tilde{\chi}_1^\pm} \gtrsim 235$ GeV, $m_{\tilde{\chi}_3^0} \gtrsim 515$ GeV, $m_{\tilde{\chi}_4^0} \gtrsim 525$ GeV, $m_{\tilde{\chi}_2^\pm} \gtrsim 530$ GeV, $m_{\tilde{\nu}_\mu} \gtrsim 235$ GeV, $m_{\tilde{\mu}_1} \gtrsim 215$ GeV, and $m_{\tilde{\mu}_2} \gtrsim 250$ GeV, where $\tilde{\chi}_2^0$ and $\tilde{\chi}_1^\pm$ are wino-dominated when they are lighter than about 500 GeV. These bounds are far beyond the reach of the LEP experiments in searching for supersymmetry and have not been acquired before. In addition, we illuminate how some parameter spaces of the MSSM have been tested at the LHC and provide five scenarios in which the theory coincides with the LHC restrictions. Once the muon g-2 anomaly is confirmed to originate from supersymmetry, this research may serve as a guide to explore the characteristics of the MSSM in future experiments.

DOI: 10.1103/PhysRevD.108.115010

I. INTRODUCTION

As the cornerstone of particle physics, the Standard Model (SM) has encapsulated our best understanding of fundamental particles and forces. Although it is well tested by many experimental results, there are still unsolved puzzles, such as the quadratic divergence in the Higgs squared mass and the absence of dark matter (DM) candidates. Historically, these puzzles were viewed as the robust evidence of new physics beyond the SM, and looking for mechanisms to circumvent them was the model-building guideline. Supersymmetry (SUSY) is the most promising among the new physics theories due to its elegant structure and remarkable advantages in solving these puzzles [1–4].

To date, rich information about SUSY has been accumulated due to the rapid progress of particle physics experiments in recent years. The run-II data of the Large Hadron Collider (LHC) enabled scientists to explore the properties of winos, higgsinos, and scalar leptons (sleptons), which are the SUSY partners of W, Higgs, and lepton fields, respectively. It was found that wino masses up to about 1060 GeV for $m_{\tilde{\chi}_1^0} \lesssim 400$ GeV and higgsino masses up to 900 GeV for $m_{\tilde{\chi}_1^0} \lesssim 240$ GeV have been excluded in the simplified model of SUSY [5], where $\tilde{\chi}_1^0$ denotes the lightest neutralino, acting as the lightest supersymmetric particle (LSP) and thus a DM candidate under the assumption of R-parity conservation [4], and $m_{\tilde{\chi}_1^0}$ is its mass. Thedata also excluded sleptons lighter than approximately 700 GeV when the LSP was massless based on statistical methods [5,6]. Furthermore, the LUX-ZEPLIN (LZ) experiment just released its first results about the direct search for DM, where the sensitivities to spin-independent (SI) and spin-dependent (SD) cross sections of DM-nucleon scattering have reached about 6.0×10^{-48} cm^2 and 1.0×10^{-42} cm^2, respectively, for the DM mass around 30 GeV [7]. These unprecedented precision values strongly limit the DM coupling to the SM particles, which are determined by SUSY parameters. In addition, the

[*]Corresponding author: mel18@foxmail.com
[†]heyangle@htu.edu.cn
[‡]yueyuanfang@htu.edu.cn
[§]dz481655@gmail.com

combined measurement of the muon anomalous magnetic moment, $a_\mu \equiv (g-2)_\mu/2$, by the E821 experiment at the Brookhaven National Laboratory (BNL) [8] and the E989 experiment at Fermilab [9] indicates a 4.2σ discrepancy from the SM's prediction [10–30]. Although this difference may have been induced by the uncertainties in calculating the hadronic contribution to the moment, as revealed by the recent lattice simulation of the BMW collaboration [31], it was widely speculated to arise from new physics (see, e.g., Ref. [32] and the references therein). Along this direction, it is remarkable that once the difference is confirmed to originate from SUSY effects, salient features of the theory, e.g., the mass spectra of the electroweakinos and sleptons, can be inferred [33–94].

Given that SUSY predictions on these experimental results rely on different theoretical inputs, it is essential to collectively study their impacts on the minimal supersymmetric standard model (MSSM), which is the most economical realization of SUSY in particle physics [2,95,96]. For this purpose, we organize this study as follows. In Sec. II, we briefly introduce the basics of the MSSM, including its DM physics, the SUSY contribution to a_μ, the signals of SUSY particles (sparticles) at the LHC, and the strategy to search for them. In Sec. III, we perform a sophisticated scan over the broad parameter space of the MSSM and clarify how the MSSM remains consistent with the experimental results. Finally, we draw conclusions in Sec. IV.

II. THEORETICAL PRELIMINARIES OF MSSM

The following superpotential of the MSSM was given in Refs. [2,95]:

$$W = -Y_d \hat{q}\cdot\hat{H}_d\hat{d} - Y_e\hat{l}\cdot\hat{H}_d\hat{e} + Y_u\hat{q}\cdot\hat{H}_u\hat{u} + \mu\hat{H}_u\cdot\hat{H}_d, \quad (2.1)$$

where the superfields $\hat{q}$ and $\hat{l}$ are left-handed SU(2) doublets for quarks and leptons, respectively, and $\hat{u}$, $\hat{d}$, and $\hat{e}$ are right-handed singlets for the fermions. The scalar components of the Higgs doublet superfields, $\hat{H}_u$ and $\hat{H}_d$, are given by $H_u = (H_u^+, H_u^0)$ and $H_d = (H_d^0, H_d^-)$, respectively, and their product is defined by $H_u \cdot H_d = (H_u^+ H_d^- - H_u^0 H_d^0)$. The first three terms in the superpotential represent the Yukawa couplings of the quark and lepton fields, and the last term is responsible for the higgsino mass.

The MSSM predicts two CP-even Higgs bosons, h and H, one CP-odd Higgs boson A, and a pair of charged Higgs boson $H^\pm = \cos\beta H_u^\pm + \sin\beta H_d^\pm$ in the Higgs sector [95,96]. Among these states, h denotes the SM-like scalar discovered at the LHC with $m_h \simeq 125$ GeV, and the neutral states H and A are approximately degenerate with $H^\pm$ in mass. The LHC search for non-SM-like Higgs bosons has obtained model-independent upper limits on the production rates of H, A, and $H^\pm$ (see, e.g., Refs. [97,98]), indicating that they should be massive. The electroweakino sector of the MSSM consists of four neutralinos and two pairs of charginos [95], denoted by $\tilde{\chi}_i^0$ with $i = 1, 2, 3, 4$ and $\tilde{\chi}_j^\pm$ with $j = 1, 2$, respectively, in this work. The neutralinos are superpositions of bino ($\tilde{B}$), wino ($\tilde{W}^0$), and two higgsino fields ($\tilde{H}_d^0$ and $\tilde{H}_u^0$), and they are Majorana fermions. By contrast, the left-handed and right-handed components of the chargino $\tilde{\chi}_j^+$ come from the mixing of $\tilde{W}^+$ with $\tilde{H}_u^+$ and $\tilde{W}^-$ with $\tilde{H}_d^-$ respectively, and $\tilde{\chi}_j^\pm$ are Dirac fermions. By convention, the neutralinos as mass eigenstates are labeled in an ascending mass order, and so are the charginos. In addition, each slepton mass eigenstate in the MSSM is associated with a definite flavor quantum number if there is no flavor mixing in the slepton sector [99,100]. The ℓ-flavored sleptons $\tilde{\ell}_i$ (i=1,2) are mixtures of chiral scalar fields $\tilde{\ell}_L$ and $\tilde{\ell}_R$. Given that the mixing is usually small, we also denote $\tilde{\ell}_i$ by its dominant component sometimes to facilitate our discussion.

A. DM physics in MSSM

On the premise of explaining both the measured DM density and the muon g-2 anomaly, the DM candidate in the MSSM must be the bino-dominated lightest neutralino [101].[1] It achieves the measured density through the coannihilation with wino-dominated electroweakinos or sleptons, or through the Z- or h-mediated resonant annihilation [104]. In the coannihilation case, the reactions $S_iS_j \to XX'$, where S_iS_j may be any of LSP-LSP, LSP-NLSP (next-to-lightest supersymmetric particle), and NLSP-NLSP annihilation states and XX' denotes SM particles, contribute to the density [105,106]. The effective annihilation rate at a temperature T is then given by Eq. (3.2) in Ref. [106]. This formula indicates that the annihilation partner has a significant effect only when the departure of its mass from the DM mass is less than about 10%. The resonant annihilation is distinct in that the density is very sensitive to the splitting between $2|m_{\tilde{\chi}_1^0}|$ and the mediator's mass [104]. The weaker the DM coupled to the mediator, the smaller the splitting must be to achieve the measured density. Evidently, this situation requires the fine-tuning of the theoretical parameters.

The cross sections of the DM-nucleon scattering take the following form [107–109]

[1] In the case that the lightest left-handed sneutrino acts as a DM candidate, its interaction with the Z-boson predicts a much smaller density than its measured value, i.e., $\Omega h^2 \ll 0.12$, and meanwhile an unacceptably large DM-nucleon scattering rate [102]. For the wino- or higgsino-dominated DM case, the density is below 10^{-3} by our calculation. These cases were surveyed in the MSSM to explain the muon g-2 anomaly in Ref. [103].

$$\sigma^{\rm SI}_{\tilde{\chi}^0_1-N} \simeq 5\times10^{-45}\ {\rm cm}^2 \times \left(\frac{F^N_u+F^N_d}{0.28}\right)^2 \times \left\{\frac{F^N_u}{F^N_u+F^N_d}\left[\frac{\cos\alpha}{\sin\beta}\left(\frac{C_{\tilde{\chi}^0_1\tilde{\chi}^0_1 h}}{0.1}\right)\left(\frac{125\ {\rm GeV}}{m_h}\right)^2+\frac{\sin\alpha}{\sin\beta}\left(\frac{C_{\tilde{\chi}^0_1\tilde{\chi}^0_1 H}}{0.1}\right)\left(\frac{125\ {\rm GeV}}{m_H}\right)^2\right]\right.$$
$$\left.+\frac{F^N_d}{F^N_u+F^N_d}\times\left[-\frac{\sin\alpha}{\cos\beta}\left(\frac{C_{\tilde{\chi}^0_1\tilde{\chi}^0_1 h}}{0.1}\right)\left(\frac{125\ {\rm GeV}}{m_h}\right)^2+\frac{\cos\alpha}{\cos\beta}\left(\frac{C_{\tilde{\chi}^0_1\tilde{\chi}^0_1 H}}{0.1}\right)\left(\frac{125\ {\rm GeV}}{m_H}\right)^2\right]\right\}^2, \tag{2.2}$$

$$\sigma^{\rm SD}_{\tilde{\chi}^0_1-N} \simeq C_N \times \left(\frac{C_{\tilde{\chi}^0_1\tilde{\chi}^0_1 Z}}{0.1}\right)^2, \tag{2.3}$$

where F^N_u and F^N_d denote the normalized up-type and down-type quark contributions to the nucleon mass, respectively, and C_N is related with the nucleon spin with $C_p \simeq 1.8\times10^{-40}$ cm^2 for protons and $C_n \simeq 1.4\times10^{-40}$ cm^2 for neutrons. α is the mixing angle of the CP-even Higgs states satisfying $\alpha \simeq \beta - \pi/2$ in the large m_A limit [96], and β is defined by the ratio of the Higgs vacuum expectation values, namely $\tan\beta \equiv v_u/v_d$. $C_{\tilde{\chi}^0_1\tilde{\chi}^0_1 h}$, $C_{\tilde{\chi}^0_1\tilde{\chi}^0_1 H}$, and $C_{\tilde{\chi}^0_1\tilde{\chi}^0_1 Z}$ represent the DM couplings to the Higgs bosons h and H, and Z-boson, respectively. In the series expansion with m_Z/μ as a variable, they are approximated by [110–113]:

$$C_{\tilde{\chi}^0_1\tilde{\chi}^0_1 h} \simeq e\tan\theta_W \frac{m_Z}{\mu(1-m^2_{\tilde{\chi}^0_1}/\mu^2)}\left(\cos(\beta+\alpha)+\sin(\beta-\alpha)\frac{m_{\tilde{\chi}^0_1}}{\mu}\right)$$
$$\simeq e\tan\theta_W \frac{m_Z}{\mu(1-m^2_{\tilde{\chi}^0_1}/\mu^2)}\left(\sin 2\beta+\frac{m_{\tilde{\chi}^0_1}}{\mu}\right), \tag{2.4}$$

$$C_{\tilde{\chi}^0_1\tilde{\chi}^0_1 H} \simeq e\tan\theta_W \frac{m_Z}{\mu(1-m^2_{\tilde{\chi}^0_1}/\mu^2)}\left(\sin(\beta+\alpha)+\cos(\beta-\alpha)\frac{m_{\tilde{\chi}^0_1}}{\mu}\right)$$
$$\simeq -e\tan\theta_W \cos 2\beta \frac{m_Z}{\mu(1-m^2_{\tilde{\chi}^0_1}/\mu^2)}, \tag{2.5}$$

$$C_{\tilde{\chi}^0_1\tilde{\chi}^0_1 Z} \simeq \frac{e\tan\theta_W\cos 2\beta}{2}\frac{m^2_Z}{\mu^2-m^2_{\tilde{\chi}^0_1}}, \tag{2.6}$$

where θ_W is the weak mixing angle, and the DM mass $m_{\tilde{\chi}^0_1}$ relates to the bino mass M_1 by $m_{\tilde{\chi}^0_1} \simeq M_1$. Taking $F^N_u \simeq F^N_d \simeq 0.14$ [111] and $\tan\beta \gg 1$, one can conclude that

$$\sigma^{\rm SI}_{\tilde{\chi}^0_1-N} \simeq 1.4\times10^{-44}\ {\rm cm}^2 \times \left(\frac{m_Z}{\mu(1-m^2_{\tilde{\chi}^0_1}/\mu^2)}\right)^2\left[\left(\sin 2\beta+\frac{m_{\tilde{\chi}^0_1}}{\mu}\right)\left(\frac{125\ {\rm GeV}}{m_h}\right)^2+\frac{\tan\beta}{2}\left(\frac{125\ {\rm GeV}}{m_H}\right)^2\right]^2. \tag{2.7}$$

This formula reveals that if M_1 and μ are of the same sign and the Higgs boson H is tremendously massive, μ must be sufficiently large to be consistent with the results of the PandaX-4T experiment [114]. It also shows that if M_1 and μ are of opposite signs, which can result in the blind spots of the scattering [111,115–117], $|\mu| \sim 100$ GeV seems to be experimentally allowed. However, such a possibility has been limited by the experimental search for the SD DM-nucleon scattering because, regardless of the relative sign between M_1 and μ, a small $|\mu|$ can enhance the scattering cross section. In summary, the DM direct detection experiments alone have set a lower bound on the magnitude of μ. With the improvement of the experimental sensitivity, the bound will become tightened.

B. Muon g-2

The SUSY source of the muon g-2, $a^{\rm SUSY}_\mu$, mainly includes loops mediated by a smuon and a neutralino and those containing a muon-flavor sneutrino and a chargino [33–36]. The full one-loop contributions to $a^{\rm SUSY}_\mu$ in the MSSM are not presented here for brevity. Instead, we provide the expression of $a^{\rm SUSY}_\mu$ in the mass insertion approximation to reveal its key features [35]. Specifically, at the lowest order of the approximation, the contributions to $a^{\rm SUSY}_\mu$ are divided into four types: WHL, BHL, BHR, and BLR, where W, B, H, L, and R represent wino, bino, higgsino, and left-handed and right-handed smuon fields, respectively. They arise from the Feynman

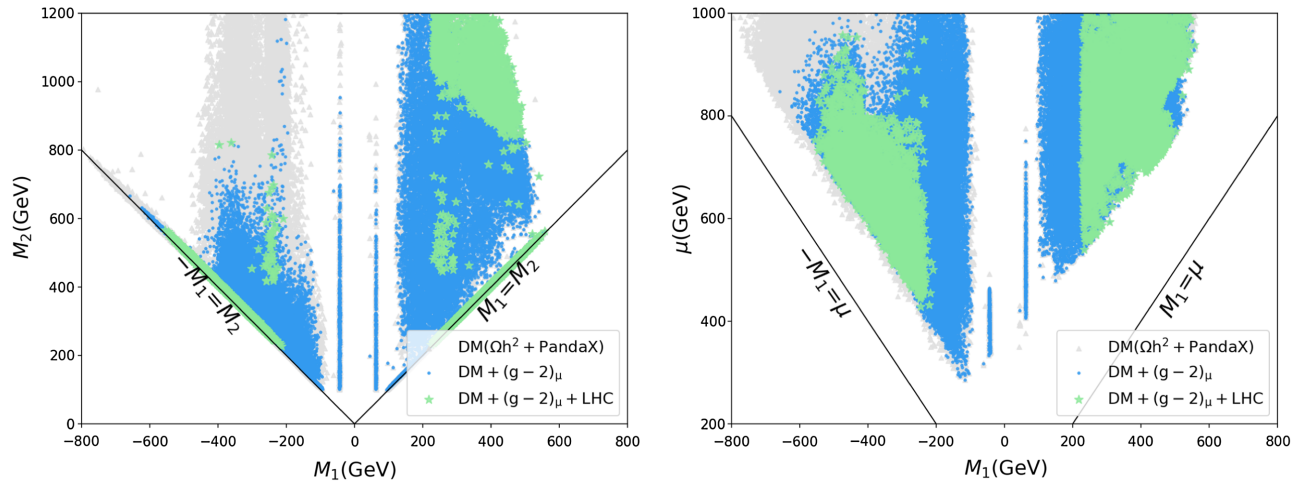

FIG. 1. Projection of the obtained samples onto $M_1 - M_2$ plane (left panel) and $M_1 - \mu$ plane (right panel). The gray triangles denote the samples that satisfy all restrictions listed in the text, in particular those from the DM relic density measured by the Planck experiment [119] and the DM direct detection of the PandaX-4T experiment [114]. The blue circles represent those that could further explain the muon g-2 anomaly at the 2σ level, and the green stars are the part of the blue circles that agree with the results from the LHC search for SUSY. Although only about one-third of the blue circles were studied by the simulations in this work (see the research strategy in the last subsection), the shape of the green areas is unlikely to significantly change. We verified this point by randomly selecting several thousands of samples from the blue areas and simulating the LHC restrictions.

diagrams involving $\tilde{W} - \tilde{H}_d$, $\tilde{B} - \tilde{H}_d^0$, $\tilde{B} - \tilde{H}_d^0$, and $\tilde{\mu}_L - \tilde{\mu}_R$ transitions, respectively, and take the following forms [35,37,38]:

$$a_{\mu,\mathrm{WHL}}^{\mathrm{SUSY}} = \frac{\alpha_2}{8\pi}\frac{m_\mu^2 M_2 \mu \tan\beta}{m_{\tilde{\nu}_\mu}^4}\left\{2f_C\left(\frac{M_2^2}{m_{\tilde{\nu}_\mu}^2},\frac{\mu^2}{m_{\tilde{\nu}_\mu}^2}\right) - \frac{m_{\tilde{\nu}_\mu}^4}{\tilde{m}_{\tilde{\mu}_L}^4} f_N\left(\frac{M_2^2}{\tilde{m}_{\tilde{\mu}_L}^2},\frac{\mu^2}{\tilde{m}_{\tilde{\mu}_L}^2}\right)\right\}, \tag{2.8}$$

$$a_{\mu,\mathrm{BHL}}^{\mathrm{SUSY}} = \frac{\alpha_Y}{8\pi}\frac{m_\mu^2 M_1 \mu \tan\beta}{\tilde{m}_{\tilde{\mu}_L}^4} f_N\left(\frac{M_1^2}{\tilde{m}_{\tilde{\mu}_L}^2},\frac{\mu^2}{\tilde{m}_{\tilde{\mu}_L}^2}\right), \tag{2.9}$$

$$a_{\mu,\mathrm{BHR}}^{\mathrm{SUSY}} = -\frac{\alpha_Y}{4\pi}\frac{m_\mu^2 M_1 \mu \tan\beta}{\tilde{m}_{\tilde{\mu}_R}^4} f_N\left(\frac{M_1^2}{\tilde{m}_{\tilde{\mu}_R}^2},\frac{\mu^2}{\tilde{m}_{\tilde{\mu}_R}^2}\right), \tag{2.10}$$

$$a_{\mu,\mathrm{BLR}}^{\mathrm{SUSY}} = \frac{\alpha_Y}{4\pi}\frac{m_\mu^2 M_1 \mu \tan\beta}{M_1^4} f_N\left(\frac{\tilde{m}_{\tilde{\mu}_L}^2}{M_1^2},\frac{\tilde{m}_{\tilde{\mu}_R}^2}{M_1^2}\right), \tag{2.11}$$

where $\tilde{m}_{\tilde{\mu}_L}$ and $\tilde{m}_{\tilde{\mu}_R}$ are soft-breaking masses for left-handed and right-handed smuon fields, respectively, at the slepton mass scale, and they are approximately equal to slepton masses. The loop functions are given by

$$f_C(x,y) = \frac{5-3(x+y)+xy}{(x-1)^2(y-1)^2} - \frac{2\ln x}{(x-y)(x-1)^3} + \frac{2\ln y}{(x-y)(y-1)^3}, \tag{2.12}$$

$$f_N(x,y) = \frac{-3+x+y+xy}{(x-1)^2(y-1)^2} + \frac{2x\ln x}{(x-y)(x-1)^3} - \frac{2y\ln y}{(x-y)(y-1)^3}, \tag{2.13}$$

satisfying $f_C(1,1) = 1/2$ and $f_N(1,1) = 1/6$.

The following points about a_μ^{SUSY} should be noted:

(i) If all the dimensional SUSY parameters involved in a_μ^{SUSY} take a common value M_{SUSY}, a_μ^{SUSY} is proportional to $m_\mu^2 \tan\beta / M_{\mathrm{SUSY}}^2$, indicating that the muon g-2 anomaly prefers a large $\tan\beta$ and a moderately low SUSY scale.

(ii) Unlike the "WHL," "BHL," and "BHR" contributions, which usually diminish monotonously with the increase of $|\mu|$, the "BLR" contribution is linearly proportional to μ. As a result, the tremendously massive higgsino scenario, characterized by predicting $\mu \gtrsim 30$ TeV, can yield the central value of the muon g-2 anomaly even when M_1, $M_{\tilde{\mu}_L}$, and $M_{\tilde{\mu}_R}$ are at the TeV scale [85]. In this study, we are not interested in this case since it needs severe fine tunings to predict m_Z [118].

(iii) Assuming $|\mu| < 1$ TeV, the "WHL" contribution is usually much larger than the other contributions if $\tilde{\mu}_L$ is not significantly heavier than $\tilde{\mu}_R$ [72].

(iv) The difference between the a_μ^{SUSY} values calculated by the mass insertion approximation and the full expression is less than 3%. We verified this conclusion for the green samples in Fig. 1 of this work.

(v) The two-loop (2L) contributions to a_μ, including 2L corrections to SM one-loop diagrams and those to

TABLE I. Experimental analyses of the electroweakino production processes considered in this study, which are categorized by the topologies of the supersymmetry (SUSY) signals.

Scenario	Final state	Name
$\tilde{\chi}_2^0\tilde{\chi}_1^\pm \to WZ\tilde{\chi}_1^0\tilde{\chi}_1^0$	$n\ell(n\geq 2)+nj(n\geq 0)+\mathrm{E}_\mathrm{T}^\mathrm{miss}$	CMS-SUS-20-001 (137 fb^{-1}) [6] ATLAS-2106-01676 (139 fb^{-1}) [124] CMS-SUS-17-004 (35.9 fb^{-1}) [122] CMS-SUS-16-039 (35.9 fb^{-1}) [123] ATLAS-1803-02762 (36.1 fb^{-1}) [126] ATLAS-1806-02293 (36.1 fb^{-1}) [127]
$\tilde{\chi}_2^0\tilde{\chi}_1^\pm \to \ell\tilde{\nu}\ell\tilde{\ell}$	$n\ell(n=3)+\mathrm{E}_\mathrm{T}^\mathrm{miss}$	CMS-SUS-16-039 (35.9 fb^{-1}) [123] ATLAS-1803-02762 (36.1 fb^{-1}) [126]
$\tilde{\chi}_2^0\tilde{\chi}_1^\pm \to \tilde{\tau}\nu\tilde{\ell}$	$2\ell+1\tau+\mathrm{E}_\mathrm{T}^\mathrm{miss}$	CMS-SUS-16-039 (35.9 fb^{-1}) [123]
$\tilde{\chi}_2^0\tilde{\chi}_1^\pm \to \tilde{\tau}\nu\tilde{\tau}\tau$	$3\tau+\mathrm{E}_\mathrm{T}^\mathrm{miss}$	CMS-SUS-16-039 (35.9 fb^{-1}) [123]
$\tilde{\chi}_2^0\tilde{\chi}_1^\pm \to Wh\tilde{\chi}_1^0\tilde{\chi}_1^0$	$n\ell(n\geq 1)+nb(n\geq 0)+nj(n\geq 0)+\mathrm{E}_\mathrm{T}^\mathrm{miss}$	ATLAS-1909-09226 (139 fb^{-1}) [128] CMS-SUS-17-004 (35.9 fb^{-1}) [122] CMS-SUS-16-039 (35.9 fb^{-1}) [123] ATLAS-1812-09432 (36.1 fb^{-1}) [129] CMS-SUS-16-034 (35.9 fb^{-1}) [130] CMS-SUS-16-045 (35.9 fb^{-1}) [131]
$\tilde{\chi}_1^\mp\tilde{\chi}_1^\pm \to WW\tilde{\chi}_1^0\tilde{\chi}_1^0$	$2\ell+\mathrm{E}_\mathrm{T}^\mathrm{miss}$	ATLAS-1908-08215 (139 fb^{-1}) [5] CMS-SUS-17-010 (35.9 fb^{-1}) [132]
$\tilde{\chi}_1^\mp\tilde{\chi}_1^\pm \to 2\tilde{\ell}\nu(\tilde{\nu}\ell)$	$2\ell+\mathrm{E}_\mathrm{T}^\mathrm{miss}$	ATLAS-1908-08215 (139 fb^{-1}) [5] CMS-SUS-17-010 (35.9 fb^{-1}) [132]
$\tilde{\chi}_2^0\tilde{\chi}_1^\mp \to h/ZW\tilde{\chi}_1^0\tilde{\chi}_1^0, \tilde{\chi}_1^0 \to \gamma/Z\tilde{G}$ $\tilde{\chi}_1^\pm\tilde{\chi}_1^\mp \to WW\tilde{\chi}_1^0\tilde{\chi}_1^0, \tilde{\chi}_1^0 \to \gamma/Z\tilde{G}$	$2\gamma+n\ell(n\geq 0)+nb(n\geq 0)+nj(n\geq 0)+\mathrm{E}_\mathrm{T}^\mathrm{miss}$	ATLAS-1802-03158 (36.1 fb^{-1}) [133]
$\tilde{\chi}_2^0\tilde{\chi}_1^\pm \to ZW\tilde{\chi}_1^0\tilde{\chi}_1^0, \tilde{\chi}_1^0 \to h/Z\tilde{G}$ $\tilde{\chi}_1^\pm\tilde{\chi}_1^\mp \to WW\tilde{\chi}_1^0\tilde{\chi}_1^0, \tilde{\chi}_1^0 \to h/Z\tilde{G}$ $\tilde{\chi}_2^0\tilde{\chi}_1^0 \to Z\tilde{\chi}_1^0\tilde{\chi}_1^0, \tilde{\chi}_1^0 \to h/Z\tilde{G}$ $\tilde{\chi}_1^\mp\tilde{\chi}_1^0 \to W\tilde{\chi}_1^0\tilde{\chi}_1^0, \tilde{\chi}_1^0 \to h/Z\tilde{G}$	$n\ell(n\geq 4)+\mathrm{E}_\mathrm{T}^\mathrm{miss}$	ATLAS-2103-11684 (139 fb^{-1}) [134]
$\tilde{\chi}_i^{0,\pm}\tilde{\chi}_j^{0,\mp} \to \tilde{\chi}_1^0\tilde{\chi}_1^0+\chi_\mathrm{soft} \to ZZ/H\tilde{G}\tilde{G}$	$n\ell(n\geq 2)+nb(n\geq 0)+nj(n\geq 0)+\mathrm{E}_\mathrm{T}^\mathrm{miss}$	CMS-SUS-16-039 (35.9 fb^{-1}) [123] CMS-SUS-17-004 (35.9 fb^{-1}) [122] CMS-SUS-20-001 (137 fb^{-1}) [6]
$\tilde{\chi}_i^{0,\pm}\tilde{\chi}_j^{0,\mp} \to \tilde{\chi}_1^0\tilde{\chi}_1^0+\chi_\mathrm{soft} \to HH\tilde{G}\tilde{G}$	$n\ell(n\geq 2)+nb(n\geq 0)+nj(n\geq 0)+\mathrm{E}_\mathrm{T}^\mathrm{miss}$	CMS-SUS-16-039 (35.9 fb^{-1}) [123] CMS-SUS-17-004 (35.9 fb^{-1}) [122]
$\tilde{\chi}_2^0\tilde{\chi}_1^\pm \to W^*Z^*\tilde{\chi}_1^0\tilde{\chi}_1^0$	$3\ell+\mathrm{E}_\mathrm{T}^\mathrm{miss}$	ATLAS-2106-01676 (139 fb^{-1}) [124]
$\tilde{\chi}_2^0\tilde{\chi}_1^\pm \to Z^*W^*\tilde{\chi}_1^0\tilde{\chi}_1^0$	$2\ell+nj(n\geq 0)+\mathrm{E}_\mathrm{T}^\mathrm{miss}$	ATLAS-1911-12606 (139 fb^{-1}) [125] ATLAS-1712-08119 (36.1 fb^{-1}) [135] CMS-SUS-16-048 (35.9 fb^{-1}) [136]
$\tilde{\chi}_2^0\tilde{\chi}_1^\pm+\tilde{\chi}_1^\pm\tilde{\chi}_1^\mp+\tilde{\chi}_1^\pm\tilde{\chi}_1^0$	$2\ell+nj(n\geq 0)+\mathrm{E}_\mathrm{T}^\mathrm{miss}$	ATLAS-1911-12606 (139 fb^{-1}) [125] ATLAS-1712-08119 (36.1 fb^{-1}) [135] CMS-SUS-16-048 (35.9 fb^{-1}) [136]

SUSY one-loop diagrams [39], are about −5% of the one-loop prediction [89]. These were neglected in this study.

C. LHC search for SUSY

Since some of the electroweakinos and sleptons involved in a_μ^SUSY must be moderately light to account for the anomaly [83], they are copiously produced at the LHC and thus are subjected to strong constraints from the SUSY searches at the LHC with $\sqrt{s} = 13$ TeV. These searches usually concentrate on theories with R-parity conservation [120,121], where the LSP is undetected, leading to missing energy in the final states. We implement these restrictions by scrutinizing the experimental analyses in Tables I and II. We find that the following reports are particularly critical:

(i) CMS-SUS-20-001 [6]: Search for SUSY signal containing two oppositely charged same-flavor leptons and missing transverse momentum. This

TABLE II. Same as Table I, but for the slepton production processes.

Scenario	Final state	Name
$\tilde{\ell}\tilde{\ell} \to \ell\ell\tilde{\chi}_1^0\tilde{\chi}_1^0$	$2\ell + \mathrm{E}_\mathrm{T}^\mathrm{miss}$	ATLAS-1911-12606 (139 fb^{-1}) [125] ATLAS-1712-08119 (36.1 fb^{-1}) [135] ATLAS-1908-08215 (139 fb^{-1}) [5] CMS-SUS-20-001 (137 fb^{-1}) [6] ATLAS-1803-02762 (36.1 fb^{-1}) [126] CMS-SUS-17-009 (35.9 fb^{-1}) [137]

analysis studied not only strong sparticle productions but also electroweakino productions. The lepton originated from an on-shell or off-shell Z boson in the decay chain or from the decay of the produced sleptons. For the electroweakino pair production, the wino-dominated chargino and neutralino were explored up to masses of 750 GeV and 800 GeV, respectively. For the slepton pair production, the first two-generation sleptons were explored up to a mass of 700 GeV.

(ii) CMS-SUS-16-039 and CMS-SUS-17-004 [122,123]: Search for electroweakino productions with two, three, or four leptons and missing transverse momentum ($\mathrm{E}_\mathrm{T}^\mathrm{miss}$) in the final states. One remarkable strategy of this analysis was that it included all the possible final states and defined several categories by the number of leptons in the event, their flavors, and their charges to enhance the discovery potential. In the context of simplified models, the observed limit on wino-dominated $m_{\tilde{\chi}_1^\pm}$ in the chargino-neutralino production was about 650 GeV for the WZ topology, 480 GeV for the WH topology, and 535 GeV for the mixed topology.

(iii) ATLAS-2106-01676 [124]: Search for wino- or higgsino-dominated chargino-neutralino pair productions. This analysis investigated on-shell WZ, off-shell WZ, and Wh categories in the decay chain and focused on the final state containing exactly three leptons, possible ISR jets, and $\mathrm{E}_\mathrm{T}^\mathrm{miss}$. For the wino scenario in the simplified model, the exclusion bound of $m_{\tilde{\chi}_2^0}$ was about 640 GeV for a massless $\tilde{\chi}_1^0$, and it was weakened as the mass difference between $\tilde{\chi}_2^0$ and $\tilde{\chi}_1^0$ diminished. Specifically, $\tilde{\chi}_2^0$ should be heavier than about 500 GeV for $m_{\tilde{\chi}_1^0} = 300$ GeV (the on-shell W/Z case), 300 GeV for a positive $m_{\tilde{\chi}_1^0}$ and 35 GeV $\lesssim m_{\tilde{\chi}_2^0} - m_{\tilde{\chi}_1^0} \lesssim 90$ GeV (the off-shell W/Z case), and 220 GeV when $m_{\tilde{\chi}_2^0} - m_{\tilde{\chi}_1^0} = 15$ GeV (the extreme off-shell W/Z case). By contrast, $\tilde{\chi}_2^0$ was excluded only up to a mass of 210 GeV for the off-shell W/Z case of the higgsino scenario, which occurred when $m_{\tilde{\chi}_2^0} - m_{\tilde{\chi}_1^0} = 10$ GeV or $m_{\tilde{\chi}_2^0} - m_{\tilde{\chi}_1^0} \gtrsim 35$ GeV.

(iv) ATLAS-1911-12606 [125]: Concentration on compressed mass spectra case and search for electroweakino pair or slepton pair production, with two leptons and missing transverse momentum as the final state. The results were projected onto the $\Delta m - \tilde{\chi}_2^0$ plane, where $\Delta m \equiv m_{\tilde{\chi}_2^0} - m_{\tilde{\chi}_1^0}$ for the electroweakino production. It was found that the tightest bound on the higgsino-dominated $\tilde{\chi}_2^0$ was 193 GeV in mass for $\Delta m \simeq 9.3$ GeV, and the optimum bound on the wino-dominated $\tilde{\chi}_2^0$ was 240 GeV in mass when $\Delta m \simeq 7$ GeV. Similarly, it was found that light-flavor sleptons should be heavier than about 250 GeV for $\Delta m_{\tilde{\ell}} = 10$ GeV, where $m_{\tilde{\ell}} \equiv m_{\tilde{\ell}} - m_{\tilde{\chi}_1^0}$.

Note that all the analyses were based on 139 fb^{-1} data except for the second analysis, which studied 36 fb^{-1} data.

III. COMBINED EXPERIMENTAL IMPACTS ON MSSM

This research utilized the package SARAH 4.14.3 [138–141] to build the model file of the MSSM, the codes SPHENO 4.0.4 [142,143] and FLAVORKIT [144] to generate particle mass spectra and compute low energy observables, such as a_μ^SUSY and B-physics observables, and the package MicrOMEGAs 5.0.4 [145–150] to calculate DM observables, assuming that the lightest neutralino was the sole DM candidate in the universe. Bounds from the direct search for extra Higgs bosons at the LEP, Tevatron, and LHC and the fit of h's property to LHC Higgs data were implemented by the programs HiggsBounds 5.10.2 [151–154] and HiggsSignals 2.6.2 [155–158], respectively.

A. Research strategy

The main aims of this research were to explore as many possibilities (parameter points) of the MSSM as possible, clarify how they remain consistent with current experimental results, and reveal some distinct characteristics of the theory. We carried out such a study by the following procedures:

(1) We employed the MULTINEST algorithm [159] to comprehensively scan the parameter space in Table III. The n_live parameter in the algorithm controlled the number of active points sampled in each iteration of the scan, and $n_\mathrm{live} = 10000$ was set. The

TABLE III. Parameter space explored in this study, where $\tan\beta$ was defined at the electroweak scale and the others were defined at the renormalization scale $Q = 1$ TeV. $M_{\tilde{\mu}_L}$ and $M_{\tilde{\mu}_R}$ are soft-breaking masses for left-handed and right-handed smuon fields, respectively. Other dimensional parameters not crucial to this study were fixed at 3 TeV, including the SUSY parameters for the first- and third-generation sleptons, three generation squarks (except for the soft trilinear coefficients A_t and A_b, which are assumed to be equal and change freely), and gluinos.

Parameter	Prior	Range	Parameter	Prior	Range
$\tan\beta$	Flat	$1 \sim 60$	A_t/TeV	Flat	$-5.0 \sim 5.0$
μ/TeV	Log	$0.1 \sim 1.0$	m_A/TeV	Log	$0.5 \sim 10$
M_1/TeV	Flat	$-1.0 \sim 1.0$	M_2/TeV	Log	$0.1 \sim 1.5$
$M_{\tilde{\mu}_L}$/TeV	Log	$0.1 \sim 1.0$	$M_{\tilde{\mu}_R}$/TeV	Log	$0.1 \sim 1.0$

following likelihood function was constructed to guide the scan:

$$\mathcal{L} = \mathcal{L}_{a_\mu} \times \mathcal{L}_{\text{const}}. \tag{3.1}$$

$\mathcal{L}_{a_\mu}$ is the likelihood function of the muon g-2 anomaly given by

$$\begin{aligned}\mathcal{L}_{a_\mu} &\equiv \text{Exp}\left[-\frac{1}{2}\left(\frac{a_\mu^{\text{SUSY}} - \Delta a_\mu}{\delta a_\mu}\right)^2\right] \\ &= \text{Exp}\left[-\frac{1}{2}\left(\frac{a_\mu^{\text{SUSY}} - 2.51 \times 10^{-9}}{5.9 \times 10^{-10}}\right)^2\right],\end{aligned}$$

where $\Delta a_\mu \equiv a_\mu^{\text{Exp}} - a_\mu^{\text{SM}}$ and δa_μ represent the difference between the experimental central value of a_μ and its SM prediction and the total uncertainties in determining Δa_μ, respectively [8–30]. $\mathcal{L}_{\text{const}}$ denotes the restrictions of some experiments on the theory. They included the consistency of h's properties with the LHC Higgs data at the 95% confidence level (CL) [158], the collider searches for extra Higgs bosons [154], the central value of the DM relic density from the Planck-2018 data [119] (assuming theoretical uncertainties of 20% in the density calculation), the 90% CL upper bounds of the PandaX-4T experiment on the SI DM-nucleon scattering [114] and the XENON-1T experiment on the SD scattering [160], the 2σ bounds on the branching ratios of $B \to X_s\gamma$ and $B_s \to \mu^+\mu^-$ [161], and the vacuum stability of the scalar potential consisting of the Higgs fields and the last two generations of slepton fields [162,163]. We defined $\mathcal{L}_{\text{const}} = 1$ if the restrictions were satisfied and $\mathcal{L}_{\text{const}} = \text{Exp}[-100]$ if they were not. More details of these restrictions were introduced in Refs. [72,86].

(2) We refined the samples obtained in the scan by the criteria $\mathcal{L}_{\text{const}} = 1$ and $|a_\mu^{\text{SUSY}} - \Delta a_\mu|/\delta a_\mu \leq 3$, and we projected those passing the selection onto the two-dimensional planes spanned by any two of the parameters M_1, M_2, μ, $\tilde{m}_{\tilde{\mu}_L}$, and $\tilde{m}_{\tilde{\mu}_R}$. We then concentrated on the region of the planes where the samples were sparsely distributed and performed a new scan by adjusting relevant parameter ranges and setting $n_{\text{live}} = 3000$.

(3) We iterated the last operation with all accumulated samples until the projected areas on the planes remained unchanged. At this point, we acquired 2.21×10^5 samples surviving the criteria, and about 1.7×10^5 of them could further explain the $(g\text{-}2)_\mu$ anomaly at the 2σ level.

(4) We simplified the study of the restrictions from the LHC search for SUSY. Specifically, given that the sample number was huge and the Monte Carlo simulation of each sample introduced below would cost more than one core-hour for our computing cluster, we selected some representative points and carried out the simulations. These points were stored in a specially designed sample database, achieved in the following way:
   (i) We searched for the sample with the greatest likelihood value from a database storing all the scan results.
   (ii) We constructed a hypersphere in the parameter space, which was centered around the sample with a radius of 10 GeV for M_1, M_2, and μ (note that the simulation results were more sensitive to these three parameters than the other dimensional parameters), 20 GeV for $\tilde{m}_{\tilde{\mu}_L}$ and $\tilde{m}_{\tilde{\mu}_R}$, and one unit for $\tan\beta$.
   (iii) We copied useful information of the central sample to the newly built database for simulation and sequentially deleted all samples in the hypersphere to update the initial database.
   (iv) We iterated the above operations until all the samples in the initial database were depleted.

We add that the method to dilute the dense samples was plausible because the R-value of the simulation relied heavily on both the mass spectra and the field compositions of sparticles, which determined their production cross sections and decay branching ratios. All samples in the hypersphere had similar properties in these two aspects, and the R-value of the studied point was typical for these

samples. In addition, the method paid more attention to the samples favored by the anomaly, which was the focus of this research. After requiring the representative points to explain the muon g-2 anomaly at the 2σ level, we finally acquired 58242 samples for the simulations.

(5) We surveyed the LHC restrictions on the representative points by simulating the following processes:

$$pp \to \tilde{\chi}_i^0 \tilde{\chi}_j^{\pm}, \quad i = 2,3,4,5, \quad j = 1,2; \tag{3.2}$$

$$pp \to \tilde{\chi}_i^{\pm} \tilde{\chi}_j^{\mp}, \quad i,j = 1,2; \tag{3.3}$$

$$pp \to \tilde{\chi}_i^0 \tilde{\chi}_j^0, \quad i,j = 2,3,4,5; \tag{3.4}$$

$$pp \to \tilde{\mu}_i^* \tilde{\mu}_j, \quad i,j = 1,2; \tag{3.5}$$

$$pp \to \tilde{\nu}_\mu^* \tilde{\nu}_\mu. \tag{3.6}$$

Specifically, the cross sections of these processes at $\sqrt{s} = 13$ TeV were calculated at the next-to-leading order (NLO) by the package PROSPINO2 [164], and 60000 and 40000 events were generated for the electroweakino and slepton production processes, respectively, by the package MADGRAPH_AMC@NLO [165,166]. A relevant parton shower and hadronization were completed by the program PYTHIA8 [167]. The resulting event files were then fed into the package CheckMATE2.0.29 [168–170] to calculate the R-value defined by $R \equiv \max\{S_i/S_{i,\mathrm{obs}}^{95}\}$, where S_i denotes the simulated event number of the ith SR in the analyses of Tables I and II, and $S_{i,\mathrm{obs}}^{95}$ represents its corresponding 95% confidence level upper limit. In this process, program DELPHES was encoded in CheckMATE for detector simulation [171].

As an alternative, we also used the program SMODELS2.2.1 [172] to study the LHC restrictions. We found that this program's capability to exclude SUSY points was usually weaker than that of the simulation due to its limited database and strict working prerequisites.

We clarified the reasons for studying the parameter space defined in Table III:

(i) Given that the soft-breaking masses of the three-generation squarks were fixed at 3 TeV, A_t ranging from -5 TeV to 5 TeV could provide an appropriate correction to acquire $122\ \mathrm{GeV} \lesssim m_h \lesssim 128\ \mathrm{GeV}$ by stop-mediated loops [96].

(ii) Since m_A could significantly affect the Higgs properties and the DM-nucleon scatterings, we let it vary from 0.5 TeV to 10 TeV, where the lower bound was inspired by the results of the LHC search for extra Higgs bosons [97,98] and the upper bound was chosen to be tremendously large to show the decoupling feature of the heavy Higgs bosons [96].

(iii) Motivated by the results of the LEP search for charginos[2] and the naturalness to predict Z-boson mass [118], we assumed $0.1\ \mathrm{TeV} \leq \mu \leq 1\ \mathrm{TeV}$.

(iv) Noting that the muon g-2 anomaly preferred $|m_{\tilde{\chi}_1^0}| \lesssim 650$ GeV [83], we set $|M_1| < 1$ TeV.

(v) M_2, $M_{\tilde{\mu}_L}$, and $M_{\tilde{\mu}_R}$ in the considered ranges could explain the muon g-2 anomaly at the 2σ level and simultaneously predict the measured DM relic abundance. Their lower bounds arose from the exclusion capability of the LEP experiment in searching for SUSY, and their upper bounds were motivated by our previous interpretations of the muon g-2 anomaly in the next-to-minimal supersymmetric standard model [87], which shared many features with the MSSM. If any of these parameters lay beyond the upper bounds, MSSM would become challenging to explain the muon g-2 anomaly on the premise of coinciding with the experimental results.

(vi) We adopted the same range of $\tan\beta$ as those in the latest global fits of the MSSM to various available experimental data, which the Mastercode group performed [101,173,174]. The range was also consistent with the most recent explanations of the muon g-2 anomaly in the MSSM (see, e.g., Refs. [38,78,83,175]). We noted that a large $\tan\beta$ could enhance the bottom Yukawa coupling, and the perturbativity of the theory up to the grand unification scale implied $\tan\beta \lesssim 75$ [176]. For the case of $60 \leq \tan\beta \leq 75$, unexplored in this study, the electroweakinos and smuons were preferred to be heavier than those in the present work explaining the muon g-2 anomaly. Consequently, the LHC restrictions on the theory became weak, and the conclusions of this study remained unchanged. One could acquire these conclusions from the feature of $a_\mu^{\mathrm{SUSY}} \propto \tan\beta$ and the upper left panel of Fig. 2 in this work.

B. Key features of the results

First, we studied the DM physics of the MSSM by projecting the samples acquired by the scans onto the $M_1 - M_2$ and $M_1 - \mu$ planes to obtain Fig. 1. This figure reveals the following facts:

(i) If only the restrictions from the DM physics are considered, the DM candidate is bino-dominated for $|M_1| \leq 800$ GeV. It may achieve the measured relic density by the Z-mediated resonant annihilation, the h-mediated resonant annihilation, or the

[2]The website http://lepsusy.web.cern.ch/lepsusy/Welcome.html provided the LEP results in SUSY search. They were acquired by the LEP SUSY Working Group, consisting of ALEPH, DELPHI, L3, and OPAL collaborations.

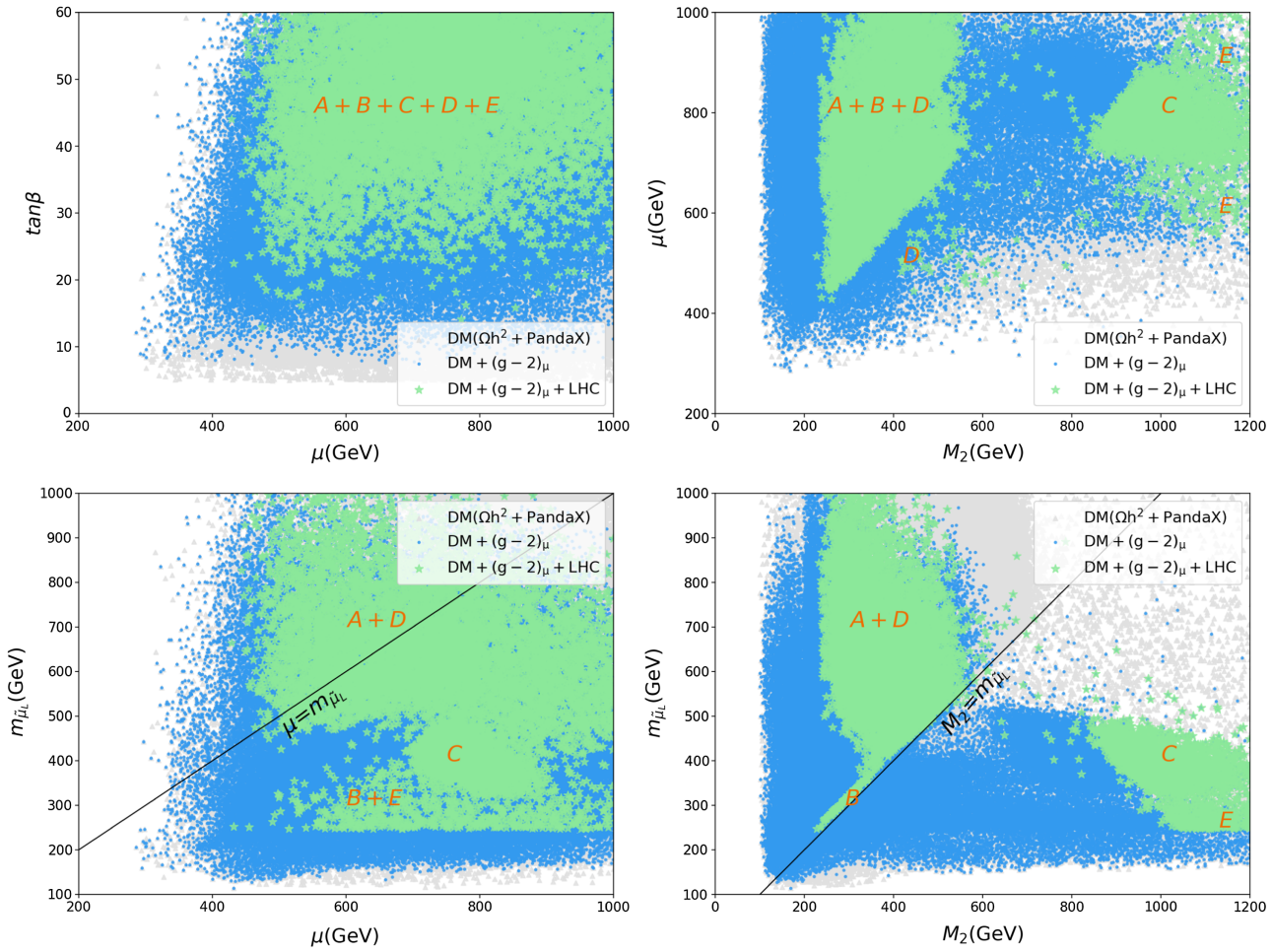

FIG. 2. Similar to Fig. 1, but showing the correlations of the parameters that $a_\mu^{\rm SUSY}$ is sensitive to. $m_{\tilde{\mu}_L}$ is the mass of the left-handed-dominated smuon, which may significantly differ from the soft-breaking parameter $M_{\tilde{\mu}_L}$ defined at $Q = 1$ TeV in Table III. Samples surviving the LHC restrictions are classified into five types, marked by A, B, C, D, and E in this figure. They are distinguished by different DM annihilation mechanisms and locations in the SUSY parameter space (see Table IV).

coannihilation with winolike electroweakinos. In addition, we will show later in Figs. 5 and 6 that it may also acquire the density by coannihilating with $\tilde{\mu}_L/\tilde{\nu}_\mu$ or $\tilde{\mu}_R$.

(ii) If the samples are further required to explain the muon g-2 anomaly at the 2σ level, $|M_1|$ is upper bounded by about 620 GeV. Furthermore, if the LHC restrictions are included, it is upper bounded by about 570 GeV.

(iii) There is a vacant region on the $M_1 - M_2$ plane, located in the ranges of 350 GeV $\lesssim M_1 \lesssim$ 570 GeV, 400 GeV $\lesssim M_2 \lesssim$ 600 GeV, and $M_1 + 30\,\text{GeV} \lesssim M_2 \lesssim M_1 + 100$ GeV. This region is distinct because winos can significantly affect the mass of $\tilde{\nu}_\mu$ by radiative corrections, and given the values of M_1 and M_2, one needs to fine-tune the soft-breaking parameter $M_{\tilde{\mu}_L}$ to predict the measured DM density by coannihilating with $\tilde{\nu}_\mu/\tilde{\mu}_L$. This situation is challenging in the scans since it easily results in $\tilde{\nu}_\mu$ as the LSP.

We add that this vacant region corresponds to the void on the bottom right corner of the $|m_{\tilde{\chi}_1^0}| - m_{\tilde{\chi}_1^\pm}$ plane in Fig. 4.

(iv) The higgsino mass μ should be larger than 300 GeV, 350 GeV, 410 GeV, and 500 GeV for the cases of $M_1 \lesssim -100$ GeV, $M_1 \simeq -m_Z/2$, $M_1 \simeq m_Z/2$, and $M_1 \gtrsim 100$ GeV, respectively. In particular, μ is more tightly limited for the possibility of $M_1 > 0$ than for the case of $M_1 < 0$, given that $|M_1|$ is fixed. These phenomena arise from the restrictions of the PandaX-4T experiment. One can understand them by the expression of $\sigma^{\rm SI}_{\tilde{\chi}_1^0 - N}$ in Eq. (2.7), noting the approximation $m_{\tilde{\chi}_1^0} \simeq M_1$ and the fact that a negative M_1 can lead to the cancelation of different contributions to the SI DM-nucleon scattering cross-section.

(v) The observables in the DM physics and the muon g-2 anomaly may prefer different parameter spaces of the MSSM, even though broad parameter regions

TABLE IV. Parameter spaces for the five types of samples in Fig. 2, where the theoretical inputs in the last five columns are in units of GeV. The second column denotes which particles $\tilde{\chi}_1^0$ will coannihilate with to acquire the measured DM density. In this aspect, Type-A and Type-B samples are different in that $m_{\tilde{\mu}_L} \gtrsim M_2 + 30$ GeV for the former and $m_{\tilde{\mu}_L} \simeq M_2$ for the latter.

Sample type	Annihilation partner	$\lvert M_1\rvert$	M_2	μ	$m_{\tilde{\mu}_L}$	$m_{\tilde{\mu}_R}$
Type-A	$\tilde{W}$	(220, 560)	(230, 600)	(430, 1000)	(350, 1000)	(300, 1000)
Type-B	$\tilde{\mu}_L$ and $\tilde{W}$	(210, 550)	(230, 600)	(430, 1000)	(240, 600)	(300, 1000)
Type-C	$\tilde{\mu}_L$	(230, 540)	(600, 1400)	(540, 1000)	(240, 550)	(230, 1000)
Type-D	$\tilde{\mu}_R$	(210, 520)	(300, 700)	(440, 1000)	(400, 1000)	(210, 1000)
Type-E	$\tilde{\mu}_R$	(230, 320)	(950, 1300)	(570, 1000)	(240, 600)	(230, 1000)

can still accommodate both. For example, a negative M_1 is disfavored by the muon g-2 anomaly in the large μ and M_2 region, because the BLR contribution to $a_\mu^{\rm SUSY}$ is negatively sizable. This case, however, can easily reproduce the results of DM experiments.

Second, we concentrate on the interplay between the muon g-2 anomaly and the LHC restrictions. As introduced in the last section, explaining the muon g-2 anomaly requires more than one sparticle to be moderately light [83]. In particular, M_2, μ, and $m_{\tilde{\mu}_L}$ cannot be very large simultaneously since the WHL contribution is usually dominant. This situation leads to sizable SUSY signals and thus strengthens the LHC restrictions. In Fig. 2, we show the correlations of any two of the three parameters, M_2, μ, and $m_{\tilde{\mu}_L}$, and also the correlation between μ and $\tan\beta$. The following distinct features are shown:

(i) The LHC restrictions have set lower bounds on the SUSY parameters: $\tan\beta \gtrsim 12$, $\mu \gtrsim 400$ GeV, $M_2 \gtrsim 230$ GeV, $m_{\tilde{\mu}_L} \gtrsim 240$ GeV, and as shown in Fig. 1, $|M_1| \gtrsim 210$ GeV.

(ii) As indicated by the top left panel, the LHC restrictions are particularly strong for $\tan\beta \lesssim 25$. The underlying reason is the muon g-2 anomaly prefers light winos, higgsinos, and left-handed-dominant smuon as $\tan\beta$ becomes small.

(iii) In the case that $\tilde{\mu}_L$ is lighter than winos and/or higgsinos, the LHC restrictions are also strong, which is reflected by the wedge-shaped excluded regions on the $M_2 - m_{\tilde{\mu}_L}$ and $\mu - m_{\tilde{\mu}_L}$ planes. This was because the heavy electroweakinos could decay into the slepton first and thus enhance the leptonic signal of the electroweakino pair production processes (compared with the case where $\tilde{\mu}_L$ is heavier than the electroweakinos). We elaborate on this point by fixing $m_{\tilde{\mu}_L} = 300$ GeV and varying M_2. For $M_2 \simeq 300$ GeV, although the total wino pair production cross sections exceeded 550 fb [177,178], there were some samples surviving the LHC constraints due to the small mass splittings between the winolike particles and $\tilde{\chi}_1^0$. In this case, the winolike particles decayed into $\tilde{\chi}_1^0$ and a soft virtual Z or W, which made the signal detection difficult. With the increase in M_2, all the samples were excluded because the winolike particles were copiously produced at the LHC due to their moderate lightness, and simultaneously the branching ratios of their decays into the slepton were sizable. Specifically, we found that the ratios were always larger than 20%. With the further increase in M_2, the wino pair production rates rapidly decreased so that the LHC constraints were weakened, reflected by the appearance of the green areas at $M_2 \simeq 900$ GeV in the bottom right panel. We add that this discussion can be applied to the $\mu - m_{\tilde{\mu}_L}$ plane in the bottom left panel.

(iv) Samples consistent with the LHC restrictions can be classified into five types, distinguished by their DM annihilation mechanisms and locations in the parameter space. They are marked as A, B, C, D, and E in the figure. In Table IV, we provide the criteria of this classification. We will present benchmark points to reveal their properties and study the LHC restrictions later.

Third, we studied the impact of the LZ experiment on the MSSM. In Figs. 1 and 2, the PandaX-4T results were used to set upper bounds on the SI cross sections of the DM-nucleon scattering [114]. We utilized the LZ limits to refine the samples further, projected the selected samples onto various panels, and compared the resulting figures with their correspondence plotted with the samples in Fig. 1. The most remarkable change came from the fact that μ was more strongly limited, which was reflected in the following aspects.

(i) Given the measured DM density, the LZ experiment alone required $\mu \gtrsim 380$ GeV for $M_1 < -100$ GeV and $\mu \gtrsim 600$ GeV for $M_1 > 100$ GeV. If the restrictions from the muon g-2 anomaly and the LHC experiment were also included, the lower bounds became about 500 GeV and 630 GeV, respectively, indicating that the theory needs a tuning of $\mathcal{O}(1\%)$ to predict the Z-boson mass [118]. Compared with the restrictions from the PandaX-4T experiment, these bounds were improved by about 100 GeV.

(ii) The Z-mediated resonant annihilation became less favored because an enhanced μ reduced $C_{\tilde{\chi}_1^0\tilde{\chi}_1^0 Z}$ in

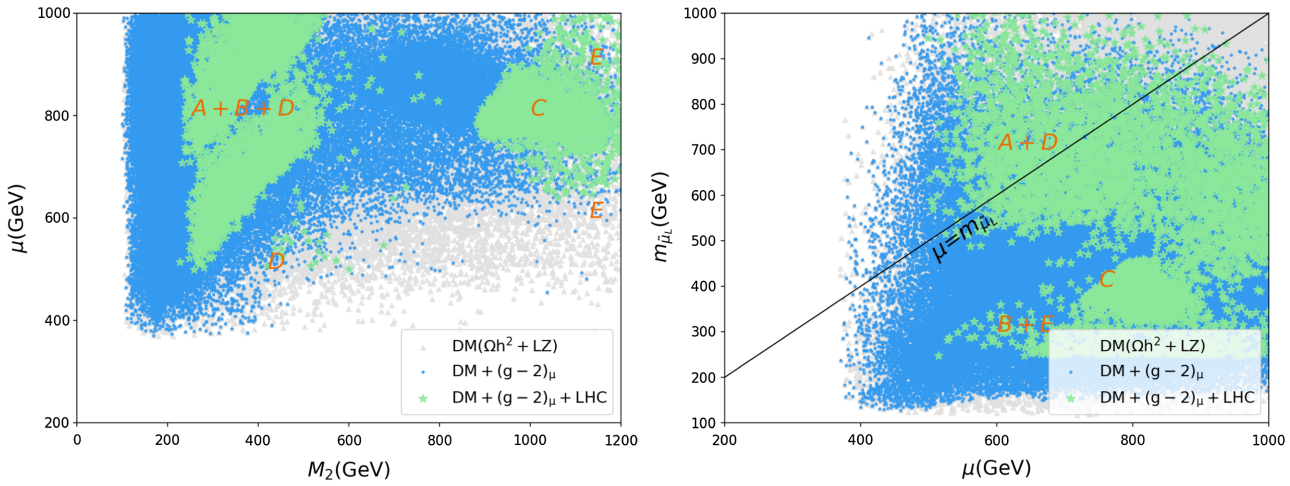

FIG. 3. Left panel: same as the upper right panel of Fig. 2, except that all the samples were required further to satisfy the LZ restrictions. Right panel: same as the left panel of this figure, except that the samples were projected onto the $\mu - m_{\tilde{\mu}_L}$ plane.

Eq. (2.6), and $2|m_{\tilde{\chi}_1^0}|$ should be closer to m_Z to obtain the measured density. This situation required the fine-tuning quantity defined in Eq. (19) of Ref. [179] to be larger than about 150 to achieve the measured density. This conclusion also applied to the h-mediated resonant annihilation. We point out that, due to the tuning, these resonant annihilation scenarios were usually missed in the scans (see, e.g., the results in Fig. 4 of this study). This point was discussed with Bayesian statistics in footnote 6 of Ref. [89].

(iii) Since the LZ constraint and the LHC restriction were sensitive to different SUSY parameters, they complemented each other in exploring the features of the MSSM. This was particularly so if one intended to explain the muon g-2 anomaly at the 2σ level. The basic reason was that μ correlated with the other parameters by the anomaly, and any enhancement of μ in a massive higgsino scenario would make winos and $\tilde{\mu}_L$ lighter to keep $a_\mu^{\rm SUSY}$ unchanged. This situation usually improved the LHC restrictions.

To show the combined effects, we projected the samples passing the LZ restrictions onto the $M_2 - \mu$ and $\mu - m_{\tilde{\mu}_L}$ planes in Fig. 3 and compared the resulting panels with their corresponding ones in Fig. 2. We also focused on the samples studied by the Monte Carlo simulations. We classified them by the dominant annihilation mechanisms of the DM, which limit of the DM experiments was set, and whether the LHC restrictions were included in this research. We presented the results in Table V. Both the figure and the table showed that the two experiments promoted each other to limit the parameter space of the MSSM.

Fourth, we surveyed the influences of these experiments on sparticle properties. We projected the samples of Fig. 1 (Fig. 3) onto the $|m_{\tilde{\chi}_1^0}| - m_{\tilde{\chi}_1^\pm}$, $|m_{\tilde{\chi}_1^0}| - m_{\tilde{\mu}_L}$, and $|m_{\tilde{\chi}_1^0}| - m_{\tilde{\mu}_R}$ planes to acquire the left (right) panels of Figs. 4–6, respectively. The classification of the samples was the same as before. From these plots, we obtained the following points:

(i) With the increase in $|m_{\tilde{\chi}_1^0}|$, the upper bounds of $m_{\tilde{\chi}_1^\pm}$ and $m_{\tilde{\mu}_L}$ decreased, and they terminated at $m_{\tilde{\chi}_1^\pm} \simeq 600$ GeV and $m_{\tilde{\mu}_L} \simeq 700$ GeV for $m_{\tilde{\chi}_1^0} \simeq 570$ GeV. This tendency was not evident for $m_{\tilde{\mu}_R}$ because $a_\mu^{\rm SUSY}$ was more sensitive to M_2, μ, and $m_{\tilde{\mu}_L}$ than to $m_{\tilde{\mu}_R}$, as indicated by Eqs. (2.8)–(2.11).

(ii) The LHC restrictions have set lower bounds on the sparticle mass spectra, which were $m_{\tilde{\chi}_1^0} \gtrsim 210$ GeV, $m_{\tilde{\chi}_1^\pm} \gtrsim 235$ GeV, $m_{\tilde{\mu}_L} \gtrsim 240$ GeV, and $m_{\tilde{\mu}_R} \gtrsim 215$ GeV in this research. The basic reason for this phenomenon is as follows: if $\tilde{\chi}_1^0$ is lighter, more missing momentum will be emitted in the sparticle

TABLE V. Numbers of the samples studied by the simulations. They were categorized by the dominant annihilation mechanisms of the DM, which limit of the DM direct detection experiments was set, and whether the LHC restrictions were included in the research.

	Before LHC constraints		After LHC constraints	
Annihilation mechanisms	PandaX	LZ	PandaX	LZ
All	58242	39657	11204	5656
$\tilde{B} - \tilde{W}$ coannihilation	31108	20123	7927	3435
$\tilde{B} - \tilde{\mu}_L - \tilde{W}$ coannihilation	10052	6622	287	174
$\tilde{B} - \tilde{\mu}_L$ coannihilation	13445	11052	2737	1884
$\tilde{B} - \tilde{\mu}_R$ coannihilation	2869	1860	253	163
$Z-$ funnel	408	0	0	0
$h-$ funnel	360	0	0	0

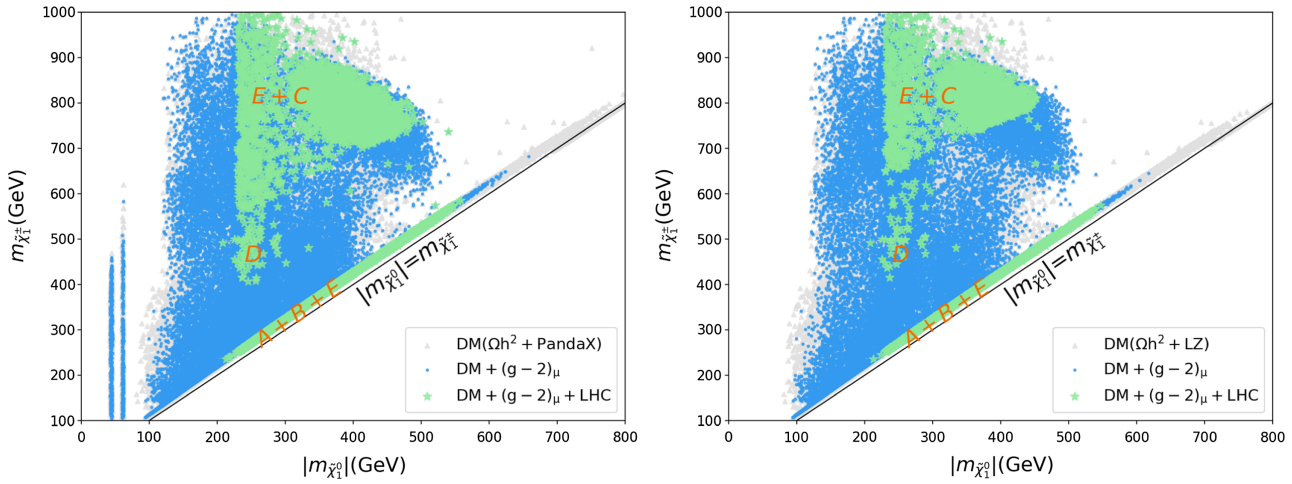

FIG. 4. Distribution of $m_{\tilde{\chi}_1^\pm}$ versus $|m_{\tilde{\chi}_1^0}|$. The left panel studies the samples in Figs. 1, while the right panel focuses on those in Fig. 3. The classification in Table IV was applied to the samples of this figure to illuminate the underlying physics.

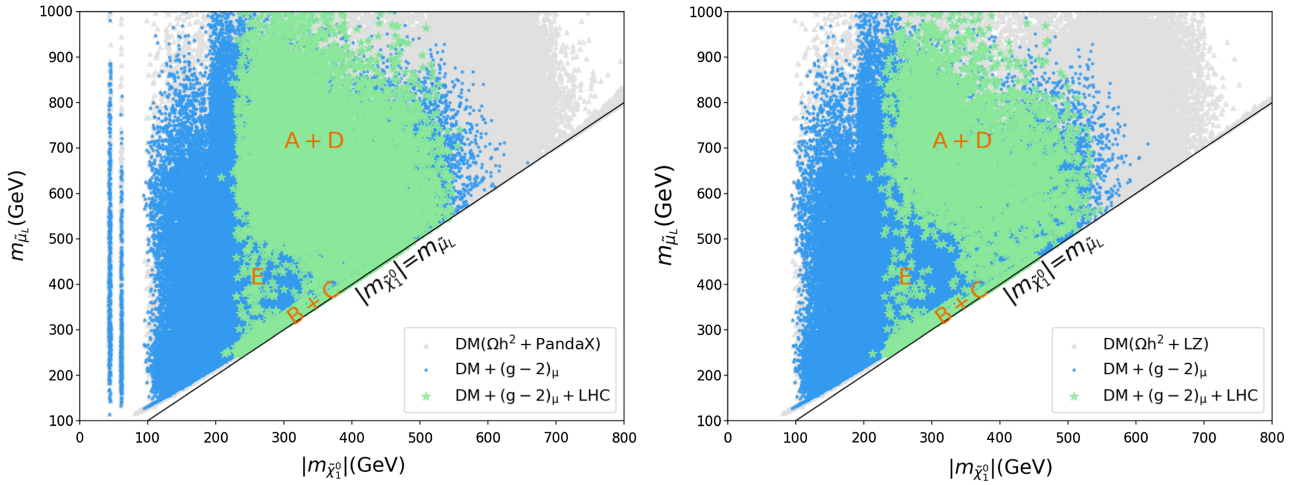

FIG. 5. Same as Fig. 4 except that it shows the distribution on the $|m_{\tilde{\chi}_1^0}| - m_{\tilde{\mu}_L}$ plane.

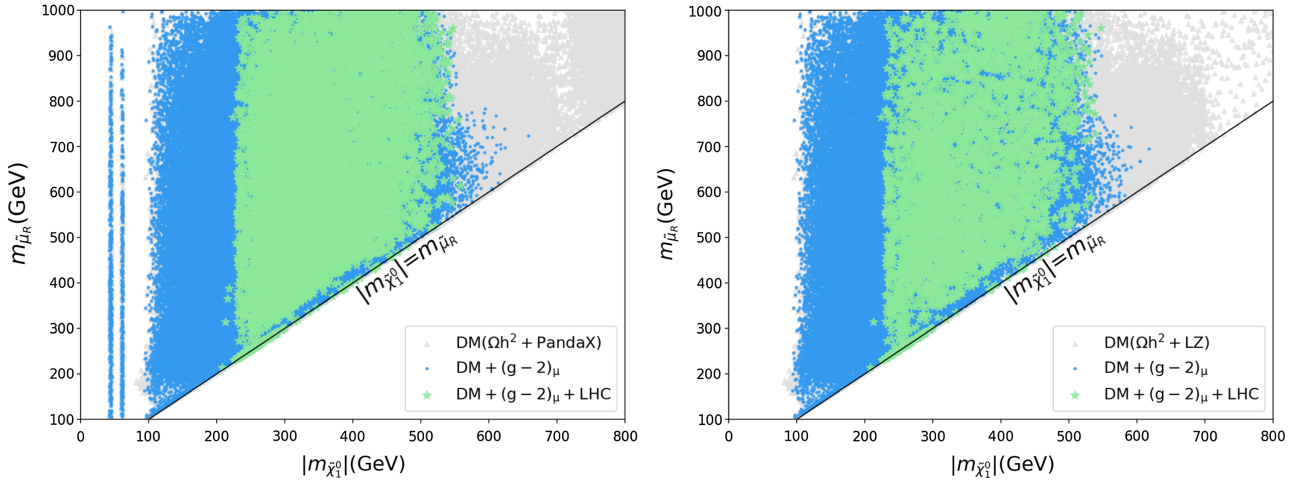

FIG. 6. Same as Fig. 4 except that the samples are displayed on the $|m_{\tilde{\chi}_1^0}| - m_{\tilde{\mu}_R}$ plane.

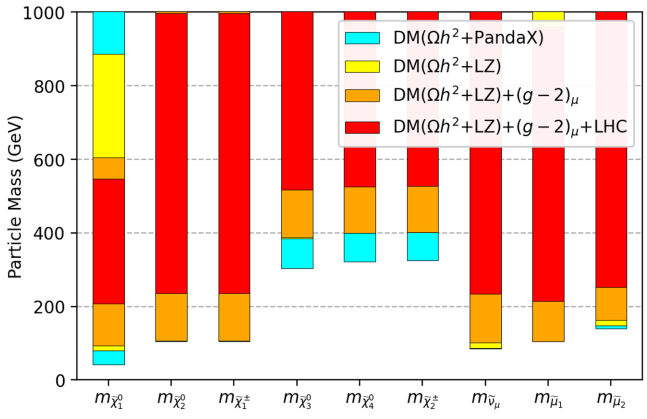

FIG. 7. Sparticle mass spectra preferred by different experiments. The cyan band was acquired from the gray samples in Fig. 1, and the yellow, orange, and red bands were from the gray, blue, and green samples in Fig. 3, respectively.

production processes at the LHC, which can improve the sensitivities of the experimental analyses; on the other hand, if sparticles other than $\tilde{\chi}_1^0$ are lighter, they will be more copiously produced at the LHC to increase the number of events containing multiple leptons. We emphasize that these bounds should be regarded as rough estimates, instead of accurate values, since far from enough samples were studied, given the broad parameter space of the MSSM.

Finally, we summarize the sparticle mass spectra preferred by different experiments in Fig. 7. This figure reveals that $570\ \text{GeV} \gtrsim m_{\tilde{\chi}_1^0} \gtrsim 210\ \text{GeV}$, $m_{\tilde{\chi}_2^0}, m_{\tilde{\chi}_1^\pm} \gtrsim 235\ \text{GeV}$, $m_{\tilde{\chi}_3^0} \gtrsim 515\ \text{GeV}$, $m_{\tilde{\chi}_4^0} \gtrsim 525\ \text{GeV}$, $m_{\tilde{\chi}_2^\pm} \gtrsim 530\ \text{GeV}$, $m_{\tilde{\nu}_\mu} \gtrsim 235\ \text{GeV}$, $950\ \text{GeV} \gtrsim m_{\tilde{\mu}_1} \gtrsim 215\ \text{GeV}$, and $m_{\tilde{\mu}_2} \gtrsim 250\ \text{GeV}$ if all the latest restrictions are considered. The lower bounds come from the LHC restrictions, and the upper bounds arise from the explanation of the muon g-2 anomaly at the 2σ level. In addition, it was verified that $\tilde{\chi}_2^0$ and $\tilde{\chi}_1^\pm$ were wino-dominated when they were lighter than about 500 GeV and $m_{\tilde{\mu}_1}$ might be either $m_{\tilde{\mu}_L}$ or $m_{\tilde{\mu}_R}$. It was also verified that $600\ \text{GeV} \gtrsim m_{\text{NLSP}} \gtrsim 220\ \text{GeV}$ and $700\ \text{GeV} \gtrsim m_{\text{NNLSP}} \gtrsim 250\ \text{GeV}$, where the NLSP and NNLSP might be either electroweakinos or sleptons. In principle, the sparticles other than $\tilde{\chi}_1^0$ and $\tilde{\mu}_1^0$ are also upper bounded in mass by the explanation of the anomaly. We do not provide these bounds since the parameter space in Table III is limited.

C. More details of LHC restrictions

Even in the simple realization of SUSY, such as the MSSM, the decay products of heavy sparticles are complex (see the benchmark points presented below). As a result, the pair productions of winos, higgsinos, $\tilde{\mu}_L$, and $\tilde{\mu}_R$ at the LHC, $pp \to \bar{\tilde{W}}\tilde{W}, \bar{\tilde{H}}\tilde{H}, \tilde{\mu}_L^*\tilde{\mu}_L, \tilde{\mu}_R^*\tilde{\mu}_R$, may contribute to the same SR of the analyses in Tables I and II. All these contributions must be suppressed for any parameter point to circumvent the LHC restrictions, which may occur in the following situations:

(1) The DM candidate is massive, compared with the results of pertinent experimental analyses. In this case, all SM particles in the final state are not energetic enough, and the missing momentum emitted in the sparticle production processes tends to be small.
(2) The mass splitting between the decaying sparticle and $\tilde{\chi}_1^0$ is less than several tens of GeV. In this compressed spectra case, the SM particles as the decay product are soft and hard to detect without a deliberate search strategy.
(3) Heavy sparticles decay by several channels with comparable branching ratios in terms of size. This situation usually leads to complicated final decay states.
(4) Sparticles are sufficiently heavy, compared with their experimental exclusion bounds in simplified models, so that their production cross sections are negligibly small.

We refer to these situations as survival mechanisms I, II, III, and IV in the following discussion. An illuminating example of situations 1 and 2 was presented in Fig. 16 of Ref. [124], which concluded that there were no LHC restrictions on winos in the $\tilde{B} - \tilde{W}$ coannihilation case if $m_{\tilde{\chi}_1^0} \gtrsim 220\ \text{GeV}$. Evidently, this bound is significantly weaker than the other searches for winos at the LHC.

To simplify the discussion of the LHC restrictions, we first classified the blue samples in Fig. 3 by the DM annihilation mechanisms, similar to what we did in Table V. Then, we only focused on the samples studied by the Monte Carlo simulations. We show in Table VI the numbers before and after simulating the LHC restrictions, the SRs that contributed to the largest R-values, and their capability to exclude the samples of each mechanism, expressed by the percentage of the total numbers in the second column. The following SRs are involved:

(i) `SR-1`: Signal regions SRG08_0j_mll and SRG07_0j_mll defined in Ref. [6]. They come from the LHC search for slepton pair production by the final state containing two opposite-sign-same-flavor (OSSF) leptons and missing transverse momentum.
(ii) `SR-2`: Signal regions SR_A44, SS15, and SR_A08 in Refs. [122,123]. They arise from the LHC search for electroweakinos with the final state containing missing transverse momentum, no jets, and two same-sign (SS) dileptons for the SS15, and three electrons, or muons that form at least one OSSF pair for the SR_A44 and SR_A08.
(iii) `SR-3`: Signal regions E-high-mm-30, S-high-mm-05, S-high-mm-10, and so on proposed in Ref. [125]. They concentrated on the electroweakinos with compressed mass spectra and investigated the sparticles' production at the LHC by the final

TABLE VI. Supplement to Table V with the SRs that contribute to the largest R-value and their capability to exclude the samples, expressed by the percentage of the total numbers in the second column. This table only counts the samples satisfying the LZ restrictions and studied by the simulations. The second and third columns denote the sample numbers before and after implementing the LHC restrictions, respectively, which are also presented in Table V. They reflect that the LHC restrictions on the $\tilde{B}-\tilde{\mu}_L-\tilde{W}$ and $\tilde{B}-\tilde{\mu}_R$ coannihilation cases are very strong. One can understand this feature from the previous discussions in this study and the benchmark points listed below. The fourth column reveals that only SR-1 from the experimental analyses in Ref. [6] and SR-2 from Refs. [122,123] played a role in excluding the $\tilde{B}-\tilde{\mu}_L$ coannihilation case, which was different from the other cases.

Annihilation mechanism	Before	After	SRs and their exclusion percentages
All	39657	5656	SR-1(23.7%), SR-2(18.5%), SR-3(12.7%), SR-4(11.6%)
$\tilde{B}-\tilde{W}$ coannihilation	20123	3435	SR-3(23.8%), SR-4(21.1%), SR-5(6.3%), SR-1(0.1%)
$\tilde{B}-\tilde{\mu}_L-\tilde{W}$ coannihilation	6622	174	SR-3(28.6%), SR-4(16.4%), SR-2(14.4%), SR-5(11.7%)
$\tilde{B}-\tilde{\mu}_L$ coannihilation	11052	1884	SR-1(52.0%), SR-2(30.4%)
$\tilde{B}-\tilde{\mu}_R$ coannihilation	1860	163	SR-2(44.0%), SR-4(32.3%), SR-3(6.2%), SR-1(0.8%)

state containing two leptons and missing transverse momentum.

(iv) SR-4: Signal regions SR_incWZoff_high_njc1, SR_WZoff_high_njd, SR_W-Z_off_high_njc, and so on defined in Ref. [124]. They studied the chargino-neutralino associated production at the LHC by the final state containing three leptons and missing transverse momentum, where the chargino and neutralino decayed into off-shell W and Z bosons, respectively.

(v) SR-5: Signal regions SR1_weakino_3high_mll_2, SR2_stop_3high_pt_1, and SR1_weakino_2media_mll_2 defined in Ref. [136]. They arose from the LHC search for new physics by the signal containing two soft oppositely charged leptons and missing transverse momentum.

These analyses revealed how the annihilation mechanisms have been tested at the LHC. In particular, Table VI shows that different SRs complement each other in doing so, and a single SR never plays a dominant role in this regard. This conclusion depends not only on the intrinsic physics of the MSSM but also on the details of these SRs. It arises from the fact that we included as many experimental analyses as possible to study the LHC restrictions, and each of them usually defined several signal regions. This situation allowed us to make good use of the experimental data to explore the parameter space of the MSSM.

Next, we illuminate how the MSSM manages to survive the LHC restriction. We looked for benchmark points from the Type-A, B, C, D, and E samples specified in Table IV and labeled them P1, P2, P3, P4, and P5, respectively. We presented their details in Tables VII–IX, and provided corresponding survival mechanisms in Table X. These mechanisms were acquired by comparing the dominant signals of the productions with pertinent experimental data. For example, the DM in P1 achieved the measured density by coannihilating with winolike particles. The applicable restriction to the wino productions came from the search for the chargino-neutralino associated production, where the chargino and neutralino decayed into off-shell W and Z bosons, respectively. The most robust results came from the analysis in Ref. [124], and they served as the guidelines of our judgment. We also provided a benchmark point, P6, located within the blue arc on the $|m_{\tilde{\chi}_1^0}|-m_{\tilde{\mu}_L}$ plane in Fig. 5, characterized by 230 GeV $\lesssim|m_{\tilde{\chi}_1^0}|\lesssim$ 350 GeV and 300 GeV $\lesssim m_{\tilde{\mu}_L}\lesssim$ 500 GeV. Our simulation indicated that it is excluded by SR_WZoff_high_njd in SR-4, which was designed for the tri-lepton signal from the decays of off-shell W and Z bosons. This point is distinct because both the wino pair production and the $\tilde{\mu}_L$ pair production contribute to this signal, and none of these processes alone can exclude this point. In addition, the program SMODELS2.2.1 is also unable to exclude it since it misses the $\tilde{\mu}_L$ contribution.

At this stage, we clarify the following points about the LHC restrictions:

(i) Throughout this study, both the theoretical uncertainties incurred in the simulations and the experimental (systematic and statistic) uncertainties were not included. Although these effects can relax the LHC restrictions, it is expected that much stronger restrictions on the MSSM will be acquired given the advent of high-luminosity LHC in the near future.

(ii) We did not include the search for charginos and neutralinos by the fully hadronic final states of W/Z and Higgs bosons with 139 fb^{-1} data [180] in this study. This search rejected large SM backgrounds by identifying high-p_T bosons with large-radius jets and jet substructure information. Thus, it was more efficient than the leptonic signal search in Ref. [124] only when winos were heavier than 600 GeV [180]. This conclusion holds in simplified models of SUSY but is never applied to this research. The reason is that the DM must coannihilate with $\tilde{\mu}_L$ or $\tilde{\mu}_R$ to achieve the measured density for $M_2\gtrsim 600$ GeV (see the results in Fig. 2), and the winolike particles

TABLE VII. Two benchmark points, P1 and P2, for Type-A and -B samples in Table IV, respectively. Both points satisfy all the restrictions listed in the text. The R-value of each point and its corresponding SR are presented in the last line of this table.

Type-A BP P1				Type-B BP P2			
μ	750.7 GeV	m_h	125.5 GeV	μ	636.8 GeV	m_h	125.2 GeV
$\tan\beta$	53.2	m_A	10359.8 GeV	$\tan\beta$	35.5	m_A	7359.7 GeV
A_t	2496.8 GeV	$m_{H^\pm}$	10337.7 GeV	A_t	2409.8 GeV	$m_{H^\pm}$	7363.2 GeV
M_1	−380.0 GeV	$m_{\tilde{\nu}_\mu}$	678.0 GeV	M_1	−292.9 GeV	$m_{\tilde{\nu}_\mu}$	316.2 GeV
M_2	386.9 GeV	$m_{\tilde{\chi}_1^0}$	−380.7 GeV	M_2	304.9 GeV	$m_{\tilde{\chi}_1^0}$	−292.7 GeV
$M_{\tilde{\mu}_L}$	550.2 GeV	$m_{\tilde{\chi}_2^0}$	404.8 GeV	$M_{\tilde{\mu}_L}$	188.4 GeV	$m_{\tilde{\chi}_2^0}$	317.4 GeV
$M_{\tilde{\mu}_R}$	972.5 GeV	$m_{\tilde{\chi}_3^0}$	−772.6 GeV	$M_{\tilde{\mu}_R}$	708.0 GeV	$m_{\tilde{\chi}_3^0}$	−656.4 GeV
$a_\mu^{\rm SUSY}$	1.95×10^{-9}	$m_{\tilde{\chi}_4^0}$	777.7 GeV	$a_\mu^{\rm SUSY}$	2.43×10^{-9}	$m_{\tilde{\chi}_4^0}$	662.0 GeV
Ωh^2	0.10	$m_{\tilde{\chi}_1^\pm}$	405.0 GeV	Ωh^2	0.12	$m_{\tilde{\chi}_1^\pm}$	317.6 GeV
$\sigma_p^{\rm SI}$	4.50×10^{-47} cm^2	$m_{\tilde{\chi}_2^\pm}$	779.6 GeV	$\sigma_p^{\rm SI}$	4.34×10^{-47} cm^2	$m_{\tilde{\chi}_2^\pm}$	664.2 GeV
$\sigma_p^{\rm SD}$	5.38×10^{-43} cm^2	$m_{\tilde{\mu}_L}$	682.2 GeV	$\sigma_p^{\rm SD}$	9.21×10^{-43} cm^2	$m_{\tilde{\mu}_L}$	325.6 GeV
		$m_{\tilde{\mu}_R}$	806.5 GeV			$m_{\tilde{\mu}_R}$	612.9 GeV
$N_{11}, N_{12}, N_{13}, N_{14}$		−0.997, −0.004, −0.075, −0.036		$N_{11}, N_{12}, N_{13}, N_{14}$		−0.996, −0.004, −0.083, −0.036	
$N_{21}, N_{22}, N_{23}, N_{24}$		0.004, 0.987, −0.140, 0.075		$N_{21}, N_{22}, N_{23}, N_{24}$		0.006, 0.985, −0.157, 0.079	
$N_{31}, N_{32}, N_{33}, N_{34}$		0.079, −0.046, −0.702, −0.706		$N_{31}, N_{32}, N_{33}, N_{34}$		0.084, −0.055, −0.700, −0.707	
$N_{41}, N_{42}, N_{43}, N_{44}$		−0.027, 0.152, 0.694, −0.703		$N_{41}, N_{42}, N_{43}, N_{44}$		−0.033, 0.166, 0.691, −0.702	
Annihilations		Fractions [%]		Annihilations		Fractions [%]	
$\tilde{B}-\tilde{W}$ Co-annihilation		89.9		$\tilde{B}-\tilde{W}/\tilde{B}-\tilde{\mu}_L$ Co-annihilation		73.0/14.5	
Decays		Branching ratios [%]		Decays		Branching ratios [%]	
$\tilde{\chi}_2^0\to\tilde{\chi}_1^0 Z^*/\tilde{\chi}_1^0 h^*$		100		$\tilde{\chi}_2^0\to\tilde{\nu}_\mu\nu_\mu$		100	
$\tilde{\chi}_3^0\to\tilde{\chi}_1^\pm W^\mp/\tilde{\chi}_2^0 Z/\tilde{\chi}_1^0 h/\tilde{\chi}_2^0 h/\tilde{\chi}_1^0 Z$		61.0/27.0/8.3/2.3/1.1		$\tilde{\chi}_3^0\to\tilde{\chi}_1^\pm W^\mp/\tilde{\chi}_2^0 Z/\tilde{\chi}_1^0 h/\tilde{\chi}_2^0 h/\tilde{\chi}_1^0 Z$		61.2/26.4/7.7/2.6/1.4	
$\tilde{\chi}_4^0\to\tilde{\chi}_1^\pm W^\mp/\tilde{\chi}_2^0 h/\tilde{\chi}_1^0 Z/\tilde{\chi}_2^0 Z/\tilde{\chi}_1^0 h$		61.3/26.2/8.3/2.8/1.0		$\tilde{\chi}_4^0\to\tilde{\chi}_1^\pm W^\mp/\tilde{\chi}_2^0 h/\tilde{\chi}_1^0 Z/\tilde{\chi}_2^0 Z/\tilde{\nu}_\mu\nu_\mu/\tilde{\chi}_1^0 h/\tilde{\mu}_L^\pm\mu^\mp$		60.9/24.7/7.6/3.3/1.4/1.2/0.9	
$\tilde{\chi}_1^\pm\to\tilde{\chi}_1^0(W^\pm)^*$		100		$\tilde{\chi}_1^\pm\to\tilde{\nu}_\mu\mu^\pm$		99.9	
$\tilde{\chi}_2^\pm\to\tilde{\chi}_2^0 W^\pm/\tilde{\chi}_1^\pm Z/\tilde{\chi}_1^\pm h/\tilde{\chi}_1^0 W^\pm$		31.0/30.1/28.6/9.9		$\tilde{\chi}_2^\pm\to\tilde{\chi}_2^0 W^\pm/\tilde{\chi}_1^\pm Z/\tilde{\chi}_1^\pm h/\tilde{\chi}_1^0 W^\pm/\tilde{\mu}_L^\pm\nu_\mu/\tilde{\nu}_\mu\mu^\pm$		30.8/29.7/27.4/9.6/1.9/0.6	
$\tilde{\mu}_L^\pm\to\tilde{\chi}_1^\pm\nu_\mu/\tilde{\chi}_2^0\mu^\pm/\tilde{\chi}_1^0\mu^\pm$		58.8/30.0/11.2		$\tilde{\mu}_L^\pm\to\tilde{\chi}_1^0\mu^\pm/\tilde{\chi}_1^\pm\nu_\mu/\tilde{\chi}_2^0\mu^\pm$		63.4/23.7/12.9	
$\tilde{\mu}_R^\pm\to\tilde{\chi}_1^0\mu^\pm/\tilde{\nu}_\mu W^\pm$		99.8/0.1		$\tilde{\mu}_R^\pm\to\tilde{\chi}_1^0\mu^\pm/\tilde{\nu}_\mu W^\pm/\tilde{\mu}_L^\pm h/\tilde{\mu}_L^\pm Z$		99.5/0.3/0.1/0.1	
$\tilde{\nu}_\mu\to\tilde{\chi}_1^\pm\mu^\mp/\tilde{\chi}_2^0\nu_\mu/\tilde{\chi}_1^0\nu_\mu$		59.8/29.4/10.8		$\tilde{\nu}_\mu\to\tilde{\chi}_1^0\nu_\mu$		100	
R value		0.37, **S-high-mm-05** in SR-3		R value		0.30, **SRG07_0j_mll** in SR-1	

TABLE VIII. Same as Table VII, but for the benchmark points of Type-C and -D samples in Table IV, labeled as P3 and P4, respectively.

Type-C BP P3				Type-D BP P4			
μ	773.0 GeV	m_h	125.6 GeV	μ	751.5 GeV	m_h	125.4 GeV
$\tan\beta$	54.1	m_A	9252.5 GeV	$\tan\beta$	58.2	m_A	2738.6 GeV
A_t	2653.7 GeV	$m_{H^\pm}$	9229.6 GeV	A_t	2485.9 GeV	$m_{H^\pm}$	2766.4 GeV
M_1	360.6 GeV	$m_{\tilde{\nu}_\mu}$	363.9 GeV	M_1	264.8 GeV	$m_{\tilde{\nu}_\mu}$	593.6 GeV
M_2	1091.0 GeV	$m_{\tilde{\chi}_1^0}$	360.7 GeV	M_2	530.4 GeV	$m_{\tilde{\chi}_1^0}$	264.1 GeV
$M_{\tilde{\mu}_L}$	113.7 GeV	$m_{\tilde{\chi}_2^0}$	785.0 GeV	$M_{\tilde{\mu}_L}$	592.0 GeV	$m_{\tilde{\chi}_2^0}$	545.0 GeV
$M_{\tilde{\mu}_R}$	1274.6 GeV	$m_{\tilde{\chi}_3^0}$	−793.7 GeV	$M_{\tilde{\mu}_R}$	263.0 GeV	$m_{\tilde{\chi}_3^0}$	−769.1 GeV
a_μ^{SUSY}	1.99×10^{-9}	$m_{\tilde{\chi}_4^0}$	1136.1 GeV	a_μ^{SUSY}	2.33×10^{-9}	$m_{\tilde{\chi}_4^0}$	782.4 GeV
Ωh^2	0.13	$m_{\tilde{\chi}_1^\pm}$	784.3 GeV	Ωh^2	0.14	$m_{\tilde{\chi}_1^\pm}$	545.2 GeV
σ_p^{SI}	6.78×10^{-47} cm^2	$m_{\tilde{\chi}_2^\pm}$	1136.2 GeV	σ_p^{SI}	4.64×10^{-47} cm^2	$m_{\tilde{\chi}_2^\pm}$	782.9 GeV
σ_p^{SD}	4.54×10^{-43} cm^2	$m_{\tilde{\mu}_L}$	372.0 GeV	σ_p^{SD}	4.16×10^{-43} cm^2	$m_{\tilde{\mu}_L}$	599.2 GeV
		$m_{\tilde{\mu}_R}$	1187.7 GeV			$m_{\tilde{\mu}_R}$	268.5 GeV
$N_{11}, N_{12}, N_{13}, N_{14}$		−0.997, 0.003, −0.071, 0.034		$N_{11}, N_{12}, N_{13}, N_{14}$		−0.998, 0.006, −0.066, 0.024	
$N_{21}, N_{22}, N_{23}, N_{24}$		0.074, 0.164, −0.698, 0.693		$N_{21}, N_{22}, N_{23}, N_{24}$		−0.023, −0.970, 0.197, −0.140	
$N_{31}, N_{32}, N_{33}, N_{34}$		0.027, −0.029, −0.706, −0.708		$N_{31}, N_{32}, N_{33}, N_{34}$		−0.030, 0.041, 0.705, 0.708	
$N_{41}, N_{42}, N_{43}, N_{44}$		−0.008, 0.986, 0.096, −0.136		$N_{41}, N_{42}, N_{43}, N_{44}$		−0.060, 0.239, 0.678, −0.692	
Annihilations		Fractions [%]		Annihilations		Fractions [%]	
$\tilde{B} - \tilde{\mu}_L$ Co-annihilation		92.6		$\tilde{B} - \tilde{\mu}_R$ Co-annihilation		95.2	
Decays		Branching ratios [%]		Decays		Branching ratios [%]	
$\tilde{\chi}_2^0 \to \tilde{\chi}_1^0 h/\tilde{\mu}_L^\pm \mu^\mp/\tilde{\chi}_1^0 Z/\tilde{\nu}_\mu \nu_\mu$		70.2/15.1/9.7/5.0		$\tilde{\chi}_2^0 \to \tilde{\chi}_1^0 h/\tilde{\chi}_1^0 Z/\tilde{\mu}_R^\pm \mu^\mp$		78.6/10.7/10.2	
$\tilde{\chi}_3^0 \to \tilde{\chi}_1^0 Z/\tilde{\chi}_1^0 h/\tilde{\mu}_L^\pm \mu^\mp/\tilde{\nu}_\mu \nu_\mu$		86.7/10.8/1.6/0.8		$\tilde{\chi}_3^0 \to \tilde{\chi}_1^\pm W^\mp/\tilde{\chi}_2^0 Z/\tilde{\chi}_1^0 Z/\tilde{\chi}_1^0 h/\tilde{\chi}_2^0 h/\tilde{\mu}_R^\pm \mu^\mp$		58.2/25.3/12.6/2.8/0.5/0.4	
$\tilde{\chi}_4^0 \to \tilde{\nu}_\mu \nu_\mu/\tilde{\mu}_L^\pm \mu^\mp/\tilde{\chi}_1^\pm W^\mp/\tilde{\chi}_3^0 Z/\tilde{\chi}_2^0 h/\tilde{\chi}_2^0 Z/\tilde{\chi}_3^0 h$		26.8/26.0/24.1/11.3/10.9/0.4/0.3		$\tilde{\chi}_4^0 \to \tilde{\chi}_1^\pm W^\mp/\tilde{\chi}_2^0 h/\tilde{\chi}_1^0 h/\tilde{\chi}_1^0 Z/\tilde{\nu}_\mu \nu_\mu/\tilde{\chi}_2^0 Z/\tilde{\mu}_L^\pm \mu^\mp/\tilde{\mu}_R^\pm \mu^\mp$		58.6/23.8/11.2/2.7/1.3/1.0/0.7/0.6	
$\tilde{\chi}_1^\pm \to \tilde{\chi}_1^0 W^\pm/\tilde{\nu}_\mu \mu^\pm/\tilde{\mu}_L^\pm \nu_\mu$		79.9/13.7/6.0		$\tilde{\chi}_1^\pm \to \tilde{\chi}_1^0 W^\pm/\tilde{\mu}_R^\pm \nu_\mu$		92.5/6.9	
$\tilde{\chi}_2^\pm \to \tilde{\mu}_L^\pm \nu_\mu/\tilde{\nu}_\mu \mu^\pm/\tilde{\chi}_2^0 W^\pm/\tilde{\chi}_1^\pm Z/\tilde{\chi}_3^0 W^\pm/\tilde{\chi}_1^\pm h$		26.3/26.1/12.8/11.9/11.7/11.2		$\tilde{\chi}_2^\pm \to \tilde{\chi}_2^0 W^\pm/\tilde{\chi}_1^\pm Z/\tilde{\chi}_1^\pm h/\tilde{\chi}_1^0 W^\pm/\tilde{\mu}_R^\pm \nu_\mu/\tilde{\nu}_\mu \mu^\pm$		31.4/28.4/24.6/13.3/1.3/0.8	
$\tilde{\mu}_L^\pm \to \tilde{\chi}_1^0 \mu^\pm$		100		$\tilde{\mu}_L^\pm \to \tilde{\chi}_1^0 \mu^\pm/\tilde{\chi}_1^\pm \nu_\mu/\tilde{\chi}_2^0 \mu^\pm/\tilde{\mu}_R^\pm h/\tilde{\mu}_R^\pm Z$		68.8/18.5/9.8/1.5/1.4	
$\tilde{\mu}_R^\pm \to \tilde{\chi}_1^0 \mu^\pm/\tilde{\chi}_2^0 \mu^\pm/\tilde{\nu}_\mu W^\pm/\tilde{\chi}_1^\pm \nu_\mu$		98.7/0.3/0.3/0.2		$\tilde{\mu}_R^\pm \to \tilde{\chi}_1^0 \mu^\pm$		100	
$\tilde{\nu}_\mu \to \tilde{\chi}_1^0 \nu_\mu$		100		$\tilde{\nu}_\mu \to \tilde{\chi}_1^0 \nu_\mu/\tilde{\chi}_1^\pm \mu^\mp/\tilde{\chi}_2^0 \nu_\mu/\tilde{\mu}_R^\pm W^\mp$		73.0/16.3/7.8/2.8	
R value		0.38, **SR_A44** in SR-2		R value		0.50, **SS15** in SR-2	

TABLE IX. Benchmark points P5 for type-E samples in Table IV and P6 located within the blue arc on the $|m_{\tilde{\chi}_1^0}| - m_{\tilde{\mu}_L}$ plane in Fig. 5. P5 satisfies all the restrictions, while P6 is excluded by the LHC search for SUSY.

Type-E BP P5				BP P6 for the curved blue area in Fig. 5			
μ	719.2 GeV	m_h	125.7 GeV	μ	551.2 GeV	m_h	125.2 GeV
$\tan\beta$	38.7	m_A	3235.4 GeV	$\tan\beta$	31.7	m_A	6279.6 GeV
A_t	2697.6 GeV	$m_{H^\pm}$	3253.2 GeV	A_t	2398.8 GeV	$m_{H^\pm}$	6284.5 GeV
M_1	277.0 GeV	$m_{\tilde{\nu}_\mu}$	310.2 GeV	M_1	−304.9 GeV	$m_{\tilde{\nu}_\mu}$	457.4 GeV
M_2	1263.2 GeV	$m_{\tilde{\chi}_1^0}$	276.0 GeV	M_2	317.5 GeV	$m_{\tilde{\chi}_1^0}$	−304.1 GeV
$M_{\tilde{\mu}_L}$	297.4 GeV	$m_{\tilde{\chi}_2^0}$	731.5 GeV	$M_{\tilde{\mu}_L}$	409.6 GeV	$m_{\tilde{\chi}_2^0}$	327.2 GeV
$M_{\tilde{\mu}_R}$	288.2 GeV	$m_{\tilde{\chi}_3^0}$	−736.8 GeV	$M_{\tilde{\mu}_R}$	755.9 GeV	$m_{\tilde{\chi}_3^0}$	−570.1 GeV
a_μ^{SUSY}	2.11×10^{-9}	$m_{\tilde{\chi}_4^0}$	1301.3 GeV	a_μ^{SUSY}	2.03×10^{-9}	$m_{\tilde{\chi}_4^0}$	578.7 GeV
Ωh^2	0.13	$m_{\tilde{\chi}_1^\pm}$	730.8 GeV	Ωh^2	0.10	$m_{\tilde{\chi}_1^\pm}$	327.5 GeV
σ_p^{SI}	5.44×10^{-47} cm^2	$m_{\tilde{\chi}_2^\pm}$	1301.5 GeV	σ_p^{SI}	1.09×10^{-46} cm^2	$m_{\tilde{\chi}_2^\pm}$	581.0 GeV
σ_p^{SD}	5.12×10^{-43} cm^2	$m_{\tilde{\mu}_L}$	321.0 GeV	σ_p^{SD}	2.04×10^{-42} cm^2	$m_{\tilde{\mu}_L}$	464.5 GeV
		$m_{\tilde{\mu}_R}$	279.6 GeV			$m_{\tilde{\mu}_R}$	700.3 GeV
$N_{11}, N_{12}, N_{13}, N_{14}$		−0.997, 0.002, −0.071, 0.028		$N_{11}, N_{12}, N_{13}, N_{14}$		−0.993, −0.007, −0.106, −0.055	
$N_{21}, N_{22}, N_{23}, N_{24}$		0.070, 0.100, −0.703, 0.700		$N_{21}, N_{22}, N_{23}, N_{24}$		0.009, 0.971, −0.206, 0.122	
$N_{31}, N_{32}, N_{33}, N_{34}$		0.030, −0.027, −0.706, −0.708		$N_{31}, N_{32}, N_{33}, N_{34}$		−0.114, 0.060, 0.697, 0.705	
$N_{41}, N_{42}, N_{43}, N_{44}$		−0.004, 0.995, 0.052, −0.090		$N_{41}, N_{42}, N_{43}, N_{44}$		0.036, −0.232, −0.679, 0.696	
Annihilations		Fractions [%]		Annihilations		Fractions [%]	
$\tilde{B}-\tilde{\mu}_R$ Co-annihilation		94.2		$\tilde{B}-\tilde{W}$ Co-annihilation		91.4	
Decays		Branching ratios [%]		Decays		Branching ratios [%]	
$\tilde{\chi}_2^0 \to \tilde{\chi}_1^0 h/\tilde{\chi}_1^0 Z/\tilde{\mu}_L^\pm \mu^\mp/\tilde{\mu}_R^\pm \mu^\mp/\tilde{\nu}_\mu \nu_\mu$		73.1/14.4/7.5/3.6/1.4		$\tilde{\chi}_2^0 \to \tilde{\chi}_1^0 Z^*/\tilde{\chi}_1^0 h^*$		100	
$\tilde{\chi}_3^0 \to \tilde{\chi}_1^0 Z/\tilde{\chi}_1^0 h/\tilde{\mu}_R^\pm \mu^\mp/\tilde{\mu}_L^\pm \mu^\mp/\tilde{\nu}_\mu \nu_\mu$		82.2/14.8/1.1/0.9/0.8		$\tilde{\chi}_3^0 \to \tilde{\chi}_1^\pm W^\mp/\tilde{\chi}_2^0 Z/\tilde{\chi}_1^0 h/\tilde{\chi}_2^0 h/\tilde{\chi}_1^0 Z$		62.1/27.0/8.1/1.4/1.1	
$\tilde{\chi}_4^0 \to \tilde{\chi}_1^\pm W^\mp/\tilde{\nu}_\mu \nu_\mu/\tilde{\mu}_L^\pm \mu^\mp/\tilde{\chi}_2^0 h/\tilde{\chi}_3^0 Z/\tilde{\chi}_2^0 Z/\tilde{\chi}_3^0 h/\tilde{\mu}_R^\pm \mu^\mp$		25.2/25.1/24.2/11.6/11.5/ 0.9/0.8/0.4		$\tilde{\chi}_4^0 \to \tilde{\chi}_1^\pm W^\mp/\tilde{\chi}_2^0 h/\tilde{\chi}_1^0 Z/\tilde{\chi}_2^0 Z/\tilde{\chi}_1^0 h/\tilde{\nu}_\mu \nu_\mu/\tilde{\mu}_L^\pm \mu^\mp$		63.6/24.0/8.2/2.2/0.8/ 0.7/0.5	
$\tilde{\chi}_1^\pm \to \tilde{\chi}_1^0 W^\pm/\tilde{\nu}_\mu \mu^\pm/\tilde{\mu}_L^\pm \nu_\mu/\tilde{\mu}_R^\pm \nu_\mu$		89.7/7.0/1.7/1.1		$\tilde{\chi}_1^\pm \to \tilde{\chi}_1^0 (W^\pm)^*$		100	
$\tilde{\chi}_2^\pm \to \tilde{\nu}_\mu \mu^\pm/\tilde{\mu}_L^\pm \nu_\mu/\tilde{\chi}_2^0 W^\pm/\tilde{\chi}_1^\pm Z/\tilde{\chi}_3^0 W^\pm/\tilde{\chi}_1^\pm h$		24.8/24.4/12.8/12.5/12.5/12.4		$\tilde{\chi}_2^\pm \to \tilde{\chi}_2^0 W^\pm/\tilde{\chi}_1^\pm Z/\tilde{\chi}_1^\pm h/\tilde{\chi}_1^0 W^\pm/\tilde{\mu}_L^\pm \nu_\mu/\tilde{\nu}_\mu \mu^\pm$		32.3/30.4/25.7/10.3/0.9/0.4	
$\tilde{\mu}_L^\pm \to \tilde{\chi}_1^0 \mu^\pm$		100		$\tilde{\mu}_L^\pm \to \tilde{\chi}_1^\pm \nu_\mu/\tilde{\chi}_2^0 \mu^\pm/\tilde{\chi}_1^0 \mu^\pm$		57.2/29.8/13.0	
$\tilde{\mu}_R^\pm \to \tilde{\chi}_1^0 \mu^\pm$		100		$\tilde{\mu}_R^\pm \to \tilde{\chi}_1^0 \mu^\pm/\tilde{\chi}_3^0 \mu^\pm$		99.5/0.2	
$\tilde{\nu}_\mu \to \tilde{\chi}_1^0 \nu_\mu$		100		$\tilde{\nu}_\mu \to \tilde{\chi}_1^\pm \mu^\mp/\tilde{\chi}_2^0 \nu_\mu/\tilde{\chi}_1^0 \nu_\mu$		59.2/28.5/12.3	
R value		0.34, **SR.A44** in SR-2		R value		1.22, **SR.WZoff.high.njd** in SR-4	

TABLE X. Survival mechanisms for the six benchmark points listed in Tables VII–IX. These mechanisms rely on both the properties of the points and the experimental search strategies. They are acquired by comparing the dominant signals of the productions with relevant experimental analyses.

	Points					
	Survival mechanism					
Production	P1	P2	P3	P4	P5	P6
$\tilde{\bar{W}}\tilde{W}$	I, II [124]	I, II [125]	III, IV [122]	I, IV [122]	IV [122]	I, II [124]
$\tilde{\bar{H}}\tilde{H}$	I, III, IV [124]	III, IV [125]	IV [122]	III, IV [122]	IV [122]	III [124]
$\tilde{\mu}_L^*\tilde{\mu}_L$	I, III, IV [6]	I, II [125]	I, II [125]	IV [6]	I, II [125]	III [6]
$\tilde{\mu}_R^*\tilde{\mu}_R$	I, IV [6]	IV [6]	IV [6]	I, II [125]	I, II [125]	IV [6]

may decay into the slepton first to enhance their leptonic signal. As a result, it is the leptonic signals that are more powerful in excluding the SUSY points. This conclusion is the same as that of the general next-to-minimal supersymmetric Standard Model (GNMSSM) studied in Ref. [89].

The latest version of SMODELS, namely SMODELS2.2.1 [172], have implemented the cut efficiencies of the hadronic analysis and relevant signal topologies in its database. We utilized this code to restrict the green samples in Fig. 1. We did not find that it had exclusion capabilities.

(iii) In some high-energy SUSY-breaking theories, $\tilde{\tau}$ may be the NLSP due to its larger Yukawa coupling than those of the first- and second-generation sleptons. In this case, heavy sparticles may decay into $\tilde{\tau}$ to change the e/μ signals of this study, and the LHC restrictions may be relaxed [46]. We will discuss such a possibility in our future work.

D. Related issues

We stress the following issues related to this research:

(i) Throughout this study, we assumed that $\tilde{\chi}_1^0$ was fully responsible for the measured density. This assumption determined that the DM is bino-dominated and approximately degenerate with winos or sleptons in mass. This has profound implications on the phenomenology of the MSSM. Relaxing this assumption usually complicates this kind of research and makes the obtained conclusions untenable. The study in Ref. [103] illustrated this point, where the authors replaced the requirement on the DM relic density in this work, i.e., $0.096 \leq \Omega h^2 \leq 0.144$, with $\Omega h^2 \leq 0.120$, and studied the restrictions of various experiments, including the DM direct detection experiments and the LHC searches for SUSY, on interpreting the muon g-2 anomaly with the MSSM. They concluded that the preferred DM candidate might be the higgsino-, wino-, or bino-dominated neutralino. In either case, the restrictions became significantly weak compared with the results of this study, and consequently, broader parameter spaces could account for the anomaly. Let us take the wino-dominated DM as an example. It was found that $m_{\tilde{\chi}_1^0}$ and μ might be as low as 100 GeV and 300 GeV, respectively, without contradicting the restrictions (see Table 2 of Ref. [103]). In this case, the relic density was around 10^{-4}, and the SI DM-nucleon scattering cross section was below 2×10^{-47} cm^2. The wino-like $\tilde{\chi}_1^\pm$ was invisible at the LHC due to its approximate degeneracy with $\tilde{\chi}_1^0$ in mass. The rates of the di- and trilepton signals from the higgsino-like electroweakino pair productions were suppressed by the multiple decay possibilities of the produced particles and thus kept consistent with the results of the LHC search for SUSY.

(ii) As pointed out by the recent lattice simulation of the BMW collaboration on the hadronic vacuum polarization (HVP) contribution to a_μ [31], the muon g-2 anomaly might arise from the uncertainties in calculating the hadronic contribution to the moment. If this speculation is corroborated, $a_\mu^{\rm SUSY}$ should be much smaller than its currently favored size, and any of the electroweakinos and $\tilde{\mu}_{L/R}$ are not necessarily light. In this case, the LHC restrictions will be relaxed significantly. For example, we recently updated the results of Ref. [109], which only studied the DM physics in GNMSSM, by including the recent LZ restrictions. We found that the analyses in Table I only excluded about 4% of the remaining samples in Fig. 2 of Ref. [109].

(iii) It has been argued that the explanations of the anomaly with the MSSM will be tested at future colliders, given that they predict some moderately light sparticles, such as $m_{\tilde{\chi}_1^0}$, $m_{\rm NLSP}$, and $m_{\rm NNLSP}$. For example, the authors of Ref. [181] compared the capabilities of different colliders to scrutinize the explanations and presented their results in Fig. 4 for the $\tilde{B}-\tilde{W}$ coannihilation case. They found that although only parts of the preferred parameter

space could be covered in the high-luminosity LHC, exhaustive coverage of the parameter space was possible at a high-energy e^+e^- collider with $\sqrt{s} \gtrsim 1$ TeV, such as ILC with $\sqrt{s} = 1$ TeV [182] and CLIC with $\sqrt{s} = 1$ TeV [183,184]. We realize that this conclusion is conditionally valid. One exception corresponds to the case that the central value of the anomaly is significantly reduced, introduced in the last item, so that multi-TeV scale supersymmetric theories are still capable of accounting for the anomaly. Another exception is the tremendously massive higgsino scenario discussed in Ref. [85], where all sparticles are heavier than 1 TeV, and in particular, the higgsino mass is typically several tens TeV. This situation is remarkable since it implies that the fine-tuning criteria will no longer serve as a valuable guideline to build new physics theories, assuming that $a_\mu^{\rm SUSY} \sim 2.0 \times 10^{-9}$ is always needed to account for the anomaly, and simultaneously no SUSY signals are detected in the future.

IV. SUMMARY

Inspired by the rapid progress of particle physics experiments in recent years, we studied their impacts on the MSSM and how the theory kept consistent with them. We are particularly interested in the recent measurement of the muon g-2 at Fermilab, the LHC search for SUSY, and the DM direct detection by the LZ experiment since they are sensitive to different parameters and complement each other to provide valuable information of the MSSM. In surveying the status of the MSSM, we utilized the MultiNest algorithm to comprehensively scan its parameter space. We adopted the muon g-2 observable to guide the scans and included the restrictions from the LHC Higgs data, DM experiments, B-physics measurements, and vacuum stability. We also examined the samples acquired from the scans by the restrictions from the LHC search for SUSY and the latest LZ experiment. The main conclusions of this research are as follows:

(i) The bino-dominated DM achieves the measured relic density by coannihilating with winolike electroweakinos, $\tilde{\mu}_L$, or $\tilde{\mu}_R$ if one intends the theory to explain the muon g-2 anomaly.

(ii) Given the measured DM density, the LZ experiment alone has required $\mu \gtrsim 380$ GeV for $M_1 < 0$ and $\mu \gtrsim 600$ GeV for $M_1 > 100$ GeV. If the restrictions from the muon g-2 anomaly and the LHC experiment are also included, the lower bounds become about 500 GeV and 630 GeV, respectively, indicating that the theory needs a tuning of $\mathcal{O}(1\%)$ to predict Z-boson mass [118]. Compared with the restriction from the PandaX-4T experiment on the SI scattering cross section, these bounds are improved by about 100 GeV. This situation makes the Z- and h-mediated resonant annihilations even more unnatural so that they are usually missed in the scans by the MULTINEST algorithm. The fundamental reason of such phenomena is the correlation between the DM physics and the electroweak symmetry breaking in the MSSM.

(iii) On the premise of explaining the muon g-2 anomaly at the 2σ level, the LHC restrictions have set bounds on the sparticle mass spectra: $m_{\tilde{\chi}_1^0} \gtrsim 210\,\text{GeV}$, $m_{\tilde{\chi}_2^0}, m_{\tilde{\chi}_1^\pm} \gtrsim 235$ GeV, $m_{\tilde{\chi}_3^0} \gtrsim 515$ GeV, $m_{\tilde{\chi}_4^0} \gtrsim 525$ GeV, $m_{\tilde{\chi}_2^\pm} \gtrsim 530$ GeV, $m_{\tilde{\nu}_\mu} \gtrsim 235$ GeV, $m_{\tilde{\mu}_1} \gtrsim 215$ GeV, and $m_{\tilde{\mu}_2} \gtrsim 250$ GeV, where $\tilde{\chi}_2^0$ and $\tilde{\chi}_1^\pm$ are wino-dominated when they are lighter than about 500 GeV and $m_{\tilde{\mu}_1}$ may be either $m_{\tilde{\mu}_L}$ or $m_{\tilde{\mu}_R}$. These bounds should be regarded as rough estimates, instead of accurate values, since the samples studied in this research are far from sufficient given the broad parameter space of the MSSM. In addition, these bounds are far beyond the reach of the LEP experiments in searching for SUSY and have not been acquired before.

The results can be interpreted as follows: if $\tilde{\chi}_1^0$ is lighter, more missing transverse energy will be emitted in the sparticle production processes at the LHC, which can improve the sensitivities of the experimental analyses; while if the sparticles other than $\tilde{\chi}_1^0$ are lighter, they will be more copiously produced at the LHC to increase the events containing multiple leptons.

(iv) We illuminate how some parameter spaces of the MSSM have been tested at the LHC in Table VI. We also list five scenarios that are consistent with the LHC restrictions in Table IV and explain why they can do so by presenting benchmark points in Tables VII–IX and their survival mechanisms in Table X.

This work extends the previous studies of the muon g-2 anomaly in the MSSM, in particular those of Refs. [83,84], by utilizing more sophisticated research strategies and surveying the LHC restrictions comprehensively. As a result, the conclusions acquired in this research are more robust than those in previous works. They exhibit the most essential characteristics of the MSSM.

Note added. Recently, the E989 experiment at Fermilab updated its measurement of muon g-2 [185]. The new world average of $a_\mu^{\rm Exp}$ showed a 5.1σ discrepancy from the SM prediction acquired by the Muon (g-2) Theory Initiative in 2020 [10], which used dispersive techniques to extract the leading-order HVP contribution from $e^+e^- \to$ hadrons data. The difference is now given by [185]

$$\Delta a_\mu \equiv a_\mu^{\rm Exp} - a_\mu^{\rm SM} = (24.9 \pm 4.8) \times 10^{-10}. \quad (4.1)$$

Compared with the previous result in 2021 [9], the central value of Δa_μ changes slightly, while its uncertainty is significantly reduced. We required the MSSM to explain the updated discrepancy at the 2σ and 3σ levels, respectively, and repeated the analyses of this work. We found the main conclusions of this study unchanged.

ACKNOWLEDGMENTS

We sincerely thank Prof. Junjie Cao for numerous helpful discussions and his great efforts to improve the manuscript. This work is supported by the National Natural Science Foundation of China (NNSFC) under Grant Nos. 12075076 and 11905044.

[1] P. Fayet and S. Ferrara, Supersymmetry, Phys. Rep. **32**, 249 (1977).
[2] H. E. Haber and G. L. Kane, The search for supersymmetry: Probing physics beyond the standard model, Phys. Rep. **117**, 75 (1985).
[3] S. P. Martin, A supersymmetry primer, Adv. Ser. Dir. High Energy Phys. **18**, 1 (1998).
[4] G. Jungman, M. Kamionkowski, and K. Griest, Supersymmetric dark matter, Phys. Rep. **267**, 195 (1996).
[5] G. Aad *et al.* (ATLAS Collaboration), Search for electroweak production of charginos and sleptons decaying into final states with two leptons and missing transverse momentum in $\sqrt{s} = 13$ TeV pp collisions using the ATLAS detector, Eur. Phys. J. C **80**, 123 (2020).
[6] A. M. Sirunyan *et al.* (CMS Collaboration), Search for supersymmetry in final states with two oppositely charged same-flavor leptons and missing transverse momentum in proton-proton collisions at $\sqrt{s} = 13$ TeV, J. High Energy Phys. 04 (2021) 123.
[7] J. Aalbers *et al.* (LZ Collaboration), First dark matter search results from the LUX-ZEPLIN (LZ) experiment, Phys. Rev. Lett. **131**, 041002 (2023).
[8] G. W. Bennett *et al.* (Muon g-2 Collaboration), Final report of the muon E821 anomalous magnetic moment measurement at BNL, Phys. Rev. D **73**, 072003 (2006).
[9] B. Abi *et al.* (Muon g-2 Collaboration), Measurement of the positive muon anomalous magnetic moment to 0.46 ppm, Phys. Rev. Lett. **126**, 141801 (2021).
[10] T. Aoyama *et al.*, The anomalous magnetic moment of the muon in the Standard Model, Phys. Rep. **887**, 1 (2020).
[11] T. Aoyama, M. Hayakawa, T. Kinoshita, and M. Nio, Complete tenth-order QED contribution to the muon g-2, Phys. Rev. Lett. **109**, 111808 (2012).
[12] T. Aoyama, T. Kinoshita, and M. Nio, Theory of the anomalous magnetic moment of the electron, Atoms **7**, 28 (2019).
[13] A. Czarnecki, W. J. Marciano, and A. Vainshtein, Refinements in electroweak contributions to the muon anomalous magnetic moment, Phys. Rev. D **67**, 073006 (2003).
[14] C. Gnendiger, D. Stöckinger, and H. Stöckinger-Kim, The electroweak contributions to $(g\text{-}2)_\mu$ after the Higgs boson mass measurement, Phys. Rev. D **88**, 053005 (2013).
[15] M. Davier, A. Hoecker, B. Malaescu, and Z. Zhang, Reevaluation of the hadronic vacuum polarisation contributions to the Standard Model predictions of the muon g-2 and $\alpha(m_Z^2)$ using newest hadronic cross-section data, Eur. Phys. J. C **77**, 827 (2017).
[16] A. Keshavarzi, D. Nomura, and T. Teubner, Muon g-2 and $\alpha(M_Z^2)$: A new data-based analysis, Phys. Rev. D **97**, 114025 (2018).
[17] G. Colangelo, M. Hoferichter, and P. Stoffer, Two-pion contribution to hadronic vacuum polarization, J. High Energy Phys. 02 (2019) 006.
[18] M. Hoferichter, B.-L. Hoid, and B. Kubis, Three-pion contribution to hadronic vacuum polarization, J. High Energy Phys. 08 (2019) 137.
[19] M. Davier, A. Hoecker, B. Malaescu, and Z. Zhang, A new evaluation of the hadronic vacuum polarisation contributions to the muon anomalous magnetic moment and to $\boldsymbol{\alpha(m_Z^2)}$, Eur. Phys. J. C **80**, 241 (2020).
[20] A. Keshavarzi, D. Nomura, and T. Teubner, The g-2 of charged leptons, $\alpha(M_Z^2)$ and the hyperfine splitting of muonium, Phys. Rev. D **101**, 014029 (2020).
[21] A. Kurz, T. Liu, P. Marquard, and M. Steinhauser, Hadronic contribution to the muon anomalous magnetic moment to next-to-next-to-leading order, Phys. Lett. B **734**, 144 (2014).
[22] K. Melnikov and A. Vainshtein, Hadronic light-by-light scattering contribution to the muon anomalous magnetic moment revisited, Phys. Rev. D **70**, 113006 (2004).
[23] P. Masjuan and P. Sánchez-Puertas, Pseudoscalar-pole contribution to the $(g_\mu\text{-}2)$: A rational approach, Phys. Rev. D **95**, 054026 (2017).
[24] G. Colangelo, M. Hoferichter, M. Procura, and P. Stoffer, Dispersion relation for hadronic light-by-light scattering: Two-pion contributions, J. High Energy Phys. 04 (2017) 161.
[25] M. Hoferichter, B.-L. Hoid, B. Kubis, S. Leupold, and S. P. Schneider, Dispersion relation for hadronic light-by-light scattering: Pion pole, J. High Energy Phys. 10 (2018) 141.
[26] A. Gérardin, H. B. Meyer, and A. Nyffeler, Lattice calculation of the pion transition form factor with $N_f = 2 + 1$ Wilson quarks, Phys. Rev. D **100**, 034520 (2019).
[27] J. Bijnens, N. Hermansson-Truedsson, and A. Rodríguez-Sánchez, Short-distance constraints for the HLbL contribution to the muon anomalous magnetic moment, Phys. Lett. B **798**, 134994 (2019).
[28] G. Colangelo, F. Hagelstein, M. Hoferichter, L. Laub, and P. Stoffer, Longitudinal short-distance constraints for the hadronic light-by-light contribution to $(g\text{-}2)_\mu$ with large-N_c Regge models, J. High Energy Phys. 03 (2020) 101.

[29] T. Blum, N. Christ, M. Hayakawa, T. Izubuchi, L. Jin, C. Jung, and C. Lehner, The hadronic light-by-light scattering contribution to the muon anomalous magnetic moment from lattice QCD, Phys. Rev. Lett. **124**, 132002 (2020).

[30] G. Colangelo, M. Hoferichter, A. Nyffeler, M. Passera, and P. Stoffer, Remarks on higher-order hadronic corrections to the muon g-2, Phys. Lett. B **735**, 90 (2014).

[31] S. Borsanyi *et al.*, Leading hadronic contribution to the muon magnetic moment from lattice QCD, Nature (London) **593**, 51 (2021).

[32] P. Athron, C. Balázs, D. H. Jacob, W. Kotlarski, D. Stöckinger, and H. Stöckinger-Kim, New physics explanations of a_μ in light of the FNAL muon g-2 measurement, J. High Energy Phys. 09 (2021) 080.

[33] S. P. Martin and J. D. Wells, Muon anomalous magnetic dipole moment in supersymmetric theories, Phys. Rev. D **64**, 035003 (2001).

[34] F. Domingo and U. Ellwanger, Constraints from the muon g-2 on the parameter space of the NMSSM, J. High Energy Phys. 07 (2008) 079.

[35] T. Moroi, The muon anomalous magnetic dipole moment in the minimal supersymmetric standard model, Phys. Rev. D **53**, 6565 (1996).

[36] W. Hollik, J. I. Illana, S. Rigolin, and D. Stockinger, One loop MSSM contribution to the weak magnetic dipole moments of heavy fermions, Phys. Lett. B **416**, 345 (1998).

[37] P. Athron, M. Bach, H. G. Fargnoli, C. Gnendiger, R. Greifenhagen, J.-h. Park, S. Paßehr, D. Stöckinger, H. Stöckinger-Kim, and A. Voigt, GM2Calc: Precise MSSM prediction for $(g-2)$ of the muon, Eur. Phys. J. C **76**, 62 (2016).

[38] M. Endo, K. Hamaguchi, S. Iwamoto, and T. Kitahara, Supersymmetric interpretation of the muon g–2 anomaly, J. High Energy Phys. 07 (2021) 075.

[39] D. Stockinger, The muon magnetic moment and supersymmetry, J. Phys. G **34**, R45 (2007).

[40] A. Czarnecki and W. J. Marciano, The muon anomalous magnetic moment: A Harbinger for 'new physics', Phys. Rev. D **64**, 013014 (2001).

[41] J. Cao, Z. Heng, D. Li, and J. M. Yang, Current experimental constraints on the lightest Higgs boson mass in the constrained MSSM, Phys. Lett. B **710**, 665 (2012).

[42] M. Endo, K. Hamaguchi, T. Kitahara, and T. Yoshinaga, Probing Bino contribution to muon g-2, J. High Energy Phys. 11 (2013) 013.

[43] Z. Kang, $H_{u,d}$-messenger couplings address the $\mu/B_\mu \setminus$ & $A_t/m^2_{H_u}$ problem and $(g\text{-}2)_\mu$ puzzle, arXiv:1610.06024.

[44] B. Zhu, R. Ding, and T. Li, Higgs mass and muon anomalous magnetic moment in the MSSM with gauge-gravity hybrid mediation, Phys. Rev. D **96**, 035029 (2017).

[45] T. T. Yanagida and N. Yokozaki, Muon g-2 in MSSM gauge mediation revisited, Phys. Lett. B **772**, 409 (2017).

[46] K. Hagiwara, K. Ma, and S. Mukhopadhyay, Closing in on the chargino contribution to the muon g-2 in the MSSM: Current LHC constraints, Phys. Rev. D **97**, 055035 (2018).

[47] P. Cox, C. Han, and T. T. Yanagida, Muon g-2 and dark matter in the minimal supersymmetric standard model, Phys. Rev. D **98**, 055015 (2018).

[48] H. M. Tran and H. T. Nguyen, GUT-inspired MSSM in light of muon g-2 and LHC results at $\sqrt{s} = 13$ TeV, Phys. Rev. D **99**, 035040 (2019).

[49] B. P. Padley, K. Sinha, and K. Wang, Natural supersymmetry, muon g-2, and the last crevices for the top squark, Phys. Rev. D **92**, 055025 (2015).

[50] A. Choudhury, L. Darmé, L. Roszkowski, E. M. Sessolo, and S. Trojanowski, Muon g-2 and related phenomenology in constrained vector-like extensions of the MSSM, J. High Energy Phys. 05 (2017) 072.

[51] N. Okada and H. M. Tran, 125 GeV Higgs boson mass and muon g-2 in 5D MSSM, Phys. Rev. D **94**, 075016 (2016).

[52] X. Du and F. Wang, NMSSM from alternative deflection in generalized deflected anomaly mediated SUSY breaking, Eur. Phys. J. C **78**, 431 (2018).

[53] X. Ning and F. Wang, Solving the muon g-2 anomaly within the NMSSM from generalized deflected AMSB, J. High Energy Phys. 08 (2017) 089.

[54] K. Wang, F. Wang, J. Zhu, and Q. Jie, The semi-constrained NMSSM in light of muon g-2, LHC, and dark matter constraints, Chin. Phys. C **42**, 103109 (2018).

[55] J.-L. Yang, T.-F. Feng, Y.-L. Yan, W. Li, S.-M. Zhao, and H.-B. Zhang, Lepton-flavor violation and two loop electroweak corrections to $(g\text{-}2)_\mu$ in the B-L symmetric SSM, Phys. Rev. D **99**, 015002 (2019).

[56] C.-X. Liu, H.-B. Zhang, J.-L. Yang, S.-M. Zhao, Y.-B. Liu, and T.-F. Feng, Higgs boson decay $h \to Z\gamma$ and muon magnetic dipole moment in the $\mu\nu$SSM, J. High Energy Phys. 04 (2020) 002.

[57] J. Cao, J. Lian, L. Meng, Y. Yue, and P. Zhu, Anomalous muon magnetic moment in the inverse seesaw extended next-to-minimal supersymmetric standard model, Phys. Rev. D **101**, 095009 (2020).

[58] J. Cao, Y. He, J. Lian, D. Zhang, and P. Zhu, Electron and muon anomalous magnetic moments in the inverse seesaw extended NMSSM, Phys. Rev. D **104**, 055009 (2021).

[59] W. Ke and P. Slavich, Higgs-mass constraints on a supersymmetric solution of the muon g-2 anomaly, Eur. Phys. J. C **82**, 89 (2022).

[60] J. L. Lamborn, T. Li, J. A. Maxin, and D. V. Nanopoulos, Resolving the $(g\text{-}2)_\mu$ discrepancy with $\mathcal{F}$-$SU(5)$ intersecting D-branes, J. High Energy Phys. 11 (2021) 081.

[61] S. Li, Y. Xiao, and J. M. Yang, Constraining CP-phases in SUSY: An interplay of muon/electron g-2 and electron EDM, Nucl. Phys. **B974**, 115629 (2022).

[62] Y. Nakai, M. Reece, and M. Suzuki, Supersymmetric alignment models for $(g\text{-}2)_\mu$, J. High Energy Phys. 10 (2021) 068.

[63] S. Li, Y. Xiao, and J. M. Yang, Can electron and muon g-2 anomalies be jointly explained in SUSY?, Eur. Phys. J. C **82**, 276 (2022).

[64] J. S. Kim, D. E. Lopez-Fogliani, A. D. Perez, and R. R. de Austri, The new $(g\text{-}2)_\mu$ and right-handed Sneutrino dark matter, Nucl. Phys. **B974**, 115637 (2022).

[65] Z. Li, G.-L. Liu, F. Wang, J. M. Yang, and Y. Zhang, Gluino-SUGRA scenarios in light of FNAL muon g-2 anomaly, J. High Energy Phys. 12 (2021) 219.

[66] W. Altmannshofer, S. A. Gadam, S. Gori, and N. Hamer, Explaining $(g\text{-}2)_\mu$ with Multi-TeV sleptons, J. High Energy Phys. 07 (2021) 118.

[67] H. Baer, V. Barger, and H. Serce, Anomalous muon magnetic moment, supersymmetry, naturalness, LHC search limits and the landscape, Phys. Lett. B **820**, 136480 (2021).

[68] M. Chakraborti, L. Roszkowski, and S. Trojanowski, GUT-constrained supersymmetry and dark matter in light of the new $(g\text{-}2)_\mu$ determination, J. High Energy Phys. 05 (2021) 252.

[69] A. Aboubrahim, M. Klasen, and P. Nath, What the Fermilab muon g-2 experiment tells us about discovering supersymmetry at high luminosity and high energy upgrades to the LHC, Phys. Rev. D **104**, 035039 (2021).

[70] S. Iwamoto, T. T. Yanagida, and N. Yokozaki, Wino-Higgsino dark matter in MSSM from the g-2 anomaly, Phys. Lett. B **823**, 136768 (2021).

[71] M. Chakraborti, S. Heinemeyer, and I. Saha, The new MUON G-2 result and supersymmetry, Eur. Phys. J. C **81**, 1114 (2021).

[72] J. Cao, J. Lian, Y. Pan, D. Zhang, and P. Zhu, Improved $(g\text{-}2)_\mu$ measurement and singlino dark matter in μ-term extended $\mathbb{Z}_3$-NMSSM, J. High Energy Phys. 09 (2021) 175.

[73] W. Yin, Muon g-2 anomaly in anomaly mediation, J. High Energy Phys. 06 (2021) 029.

[74] H.-B. Zhang, C.-X. Liu, J.-L. Yang, and T.-F. Feng, Muon anomalous magnetic dipole moment in the $\mu\nu$SSM, Chin. Phys. C **46**, 093107 (2022).

[75] M. Ibe, S. Kobayashi, Y. Nakayama, and S. Shirai, Muon g-2 in gauge mediation without SUSY CP problem, J. High Energy Phys. 07 (2021) 098.

[76] M.-D. Zheng and H.-H. Zhang, Studying the $b \to s\ell^+\ell^-$ anomalies and $(g\text{-}2)_\mu$ in R-parity violating MSSM framework with the inverse seesaw mechanism, Phys. Rev. D **104**, 115023 (2021).

[77] C. Han, Muon g-2 and CP violation in MSSM, arXiv:2104.03292.

[78] F. Wang, L. Wu, Y. Xiao, J. M. Yang, and Y. Zhang, GUT-scale constrained SUSY in light of new muon g-2 measurement, Nucl. Phys. **B970**, 115486 (2021).

[79] M. Chakraborti, S. Heinemeyer, I. Saha, and C. Schappacher, $(g\text{-}2)_\mu$ and SUSY dark matter: Direct detection and collider search complementarity, Eur. Phys. J. C **82**, 483 (2022).

[80] A. Aboubrahim, M. Klasen, P. Nath, and R. M. Syed, Tests of gluino-driven radiative breaking of the electroweak symmetry at the LHC, in *10th International Conference on New Frontiers in Physics* (2021), 12, arXiv:2112.04986.

[81] M. I. Ali, M. Chakraborti, U. Chattopadhyay, and S. Mukherjee, Muon and electron $(g\text{-}2)$ anomalies with non-holomorphic interactions in MSSM, Eur. Phys. J. C **83**, 60 (2023).

[82] K. Wang and J. Zhu, A smuon in the NMSSM confronted with the muon g-2 and SUSY searches, Chin. Phys. C **47**, 013107 (2023).

[83] M. Chakraborti, S. Heinemeyer, and I. Saha, Improved $(g\text{-}2)_\mu$ measurements and supersymmetry, Eur. Phys. J. C **80**, 984 (2020).

[84] S. Baum, M. Carena, N. R. Shah, and C. E. M. Wagner, The tiny $(g\text{-}2)$ muon wobble from small-μ supersymmetry, J. High Energy Phys. 01 (2022) 025.

[85] Y. Gu, N. Liu, L. Su, and D. Wang, Heavy bino and slepton for muon g-2 anomaly, Nucl. Phys. **B969**, 115481 (2021).

[86] J. Cao, J. Lian, Y. Pan, Y. Yue, and D. Zhang, Impact of recent $(g\text{-}2)_\mu$ measurement on the light CP-even Higgs scenario in general Next-to-Minimal Supersymmetric Standard Model, J. High Energy Phys. 03 (2022) 203.

[87] J. Cao, F. Li, J. Lian, Y. Pan, and D. Zhang, Impact of LHC probes of SUSY and recent measurement of $(g\text{-}2)_\mu$ on $\mathbb{Z}_3$-NMSSM, Sci. China Phys. Mech. Astron. **65**, 291012 (2022).

[88] F. Domingo, U. Ellwanger, and C. Hugonie, M_W, dark matter and a_μ in the NMSSM, Eur. Phys. J. C **82**, 1074 (2022).

[89] J. Cao, X. Jia, L. Meng, Y. Yue, and D. Zhang, Status of the singlino-dominated dark matter in general next-to-minimal supersymmetric standard model, J. High Energy Phys. 03 (2023) 198.

[90] L. Wang, J. M. Yang, Y. Zhang, P. Zhu, and R. Zhu, A concise review on some Higgs-related new physics models in light of current experiments, Universe **9**, 178 (2023).

[91] J. Zhao, J. Zhu, P. Zhu, and R. Zhu, Light Higgsino scenario confronted with muon g-2, Phys. Rev. D **107**, 055030 (2023).

[92] J. M. Yang, P. Zhu, and R. Zhu, A brief survey of low energy supersymmetry under current experiments, Proc. Sci. LHCP2022 (**2022**) 069.

[93] D. Sabatta, A. S. Cornell, A. Goyal, M. Kumar, B. Mellado, and X. Ruan, Connecting muon anomalous magnetic moment and multi-lepton anomalies at LHC, Chin. Phys. C **44**, 063103 (2020).

[94] J. Cao, L. Meng, and Y. Yue, Electron and muon anomalous magnetic moments in the Z3-NMSSM, Phys. Rev. D **108**, 035043 (2023).

[95] J. F. Gunion and H. E. Haber, Higgs bosons in supersymmetric models. 1., Nucl. Phys. **B272**, 1 (1986).

[96] A. Djouadi, The anatomy of electro-weak symmetry breaking. II. The Higgs bosons in the minimal supersymmetric model, Phys. Rep. **459**, 1 (2008).

[97] G. Aad *et al.* (ATLAS Collaboration), Search for heavy Higgs bosons decaying into two tau leptons with the ATLAS detector using pp collisions at $\sqrt{s} = 13$ TeV, Phys. Rev. Lett. **125**, 051801 (2020).

[98] G. Aad *et al.* (ATLAS Collaboration), Search for charged Higgs bosons decaying into a top quark and a bottom quark at $\sqrt{s} = 13$ TeV with the ATLAS detector, J. High Energy Phys. 06 (2021) 145.

[99] S. Dimopoulos and D. W. Sutter, The supersymmetric flavor problem, Nucl. Phys. **B452**, 496 (1995).

[100] F. Gabbiani, E. Gabrielli, A. Masiero, and L. Silvestrini, A complete analysis of FCNC and CP constraints in general SUSY extensions of the standard model, Nucl. Phys. **B477**, 321 (1996).

[101] E. Bagnaschi *et al.*, Likelihood analysis of the pMSSM11 in light of LHC 13-TeV data, Eur. Phys. J. C **78**, 256 (2018).

[102] T. Falk, K. A. Olive, and M. Srednicki, Heavy sneutrinos as dark matter, Phys. Lett. B **339**, 248 (1994).
[103] M. Chakraborti, S. Heinemeyer, and I. Saha, Improved $(g\text{-}2)_\mu$ measurements and wino/Higgsino dark matter, Eur. Phys. J. C **81**, 1069 (2021).
[104] K. Griest, Cross-sections, relic abundance and detection rates for neutralino dark matter, Phys. Rev. D **38**, 2357 (1988).
[105] K. Griest and D. Seckel, Three exceptions in the calculation of relic abundances, Phys. Rev. D **43**, 3191 (1991).
[106] M. J. Baker *et al.*, The coannihilation codex, J. High Energy Phys. 12 (2015) 120.
[107] S. Baum, M. Carena, N. R. Shah, and C. E. M. Wagner, Higgs portals for thermal dark matter. EFT perspectives and the NMSSM, J. High Energy Phys. 04 (2018) 069.
[108] J. Cao, L. Meng, Y. Yue, H. Zhou, and P. Zhu, Suppressing the scattering of WIMP dark matter and nucleons in supersymmetric theories, Phys. Rev. D **101**, 075003 (2020).
[109] J. Cao, D. Li, J. Lian, Y. Yue, and H. Zhou, Singlino-dominated dark matter in general NMSSM, J. High Energy Phys. 06 (2021) 176.
[110] A. Pierce, N. R. Shah, and K. Freese, Neutralino dark matter with light staus, arXiv:1309.7351.
[111] P. Huang and C. E. M. Wagner, Blind spots for neutralino dark matter in the MSSM with an intermediate m_A, Phys. Rev. D **90**, 015018 (2014).
[112] L. Calibbi, J. M. Lindert, T. Ota, and Y. Takanishi, LHC tests of light neutralino dark matter without light Sfermions, J. High Energy Phys. 11 (2014) 106.
[113] C. Cheung, M. Papucci, D. Sanford, N. R. Shah, and K. M. Zurek, NMSSM interpretation of the galactic center excess, Phys. Rev. D **90**, 075011 (2014).
[114] Y. Meng *et al.* (PandaX-4T Collaboration), Dark matter search results from the PandaX-4T commissioning run, Phys. Rev. Lett. **127**, 261802 (2021).
[115] A. Crivellin, M. Hoferichter, M. Procura, and L. C. Tunstall, Light stops, blind spots, and isospin violation in the MSSM, J. High Energy Phys. 07 (2015) 129.
[116] T. Han, F. Kling, S. Su, and Y. Wu, Unblinding the dark matter blind spots, J. High Energy Phys. 02 (2017) 057.
[117] M. Carena, J. Osborne, N. R. Shah, and C. E. M. Wagner, Supersymmetry and LHC missing energy signals, Phys. Rev. D **98**, 115010 (2018).
[118] H. Baer, V. Barger, P. Huang, and X. Tata, Natural supersymmetry: LHC, dark matter and ILC searches, J. High Energy Phys. 05 (2012) 109.
[119] N. Aghanim *et al.* (Planck Collaboration), Planck 2018 results. VI. Cosmological parameters, Astron. Astrophys. **641**, A6 (2020).
[120] P. Fayet, Spontaneously broken supersymmetric theories of weak, electromagnetic and strong interactions, Phys. Lett. B **69**, 489 (1977).
[121] G. R. Farrar and P. Fayet, Phenomenology of the production, decay, and detection of new hadronic states associated with supersymmetry, Phys. Lett. B **76**, 575 (1978).
[122] A. M. Sirunyan *et al.* (CMS Collaboration), Combined search for electroweak production of charginos and neutralinos in proton-proton collisions at $\sqrt{s} = 13$ TeV, J. High Energy Phys. 03 (2018) 160.
[123] A. M. Sirunyan *et al.* (CMS Collaboration), Search for electroweak production of charginos and neutralinos in multilepton final states in proton-proton collisions at $\sqrt{s} = 13$ TeV, J. High Energy Phys. 03 (2018) 166.
[124] G. Aad *et al.* (ATLAS Collaboration), Search for chargino–neutralino pair production in final states with three leptons and missing transverse momentum in $\sqrt{s} = 13$ TeV pp collisions with the ATLAS detector, Eur. Phys. J. C **81**, 1118 (2021).
[125] G. Aad *et al.* (ATLAS Collaboration), Searches for electroweak production of supersymmetric particles with compressed mass spectra in $\sqrt{s} = 13$ TeV pp collisions with the ATLAS detector, Phys. Rev. D **101**, 052005 (2020).
[126] M. Aaboud *et al.* (ATLAS Collaboration), Search for electroweak production of supersymmetric particles in final states with two or three leptons at $\sqrt{s} = 13$ TeV with the ATLAS detector, Eur. Phys. J. C **78**, 995 (2018).
[127] M. Aaboud *et al.* (ATLAS Collaboration), Search for chargino-neutralino production using recursive jigsaw reconstruction in final states with two or three charged leptons in proton-proton collisions at $\sqrt{s} = 13$ TeV with the ATLAS detector, Phys. Rev. D **98**, 092012 (2018).
[128] G. Aad *et al.* (ATLAS Collaboration), Search for direct production of electroweakinos in final states with one lepton, missing transverse momentum and a Higgs boson decaying into two b-jets in pp collisions at $\sqrt{s} = 13$ TeV with the ATLAS detector, Eur. Phys. J. C **80**, 691 (2020).
[129] M. Aaboud *et al.* (ATLAS Collaboration), Search for chargino and neutralino production in final states with a Higgs boson and missing transverse momentum at $\sqrt{s} =$ 13 TeV with the ATLAS detector, Phys. Rev. D **100**, 012006 (2019).
[130] A. M. Sirunyan *et al.* (CMS Collaboration), Search for new phenomena in final states with two opposite-charge, same-flavor leptons, jets, and missing transverse momentum in pp collisions at $\sqrt{s} = 13$ TeV, J. High Energy Phys. 03 (2018) 076.
[131] A. M. Sirunyan *et al.* (CMS Collaboration), Search for supersymmetry with Higgs boson to diphoton decays using the razor variables at $\sqrt{s} = 13$ TeV, Phys. Lett. B **779**, 166 (2018).
[132] A. M. Sirunyan *et al.* (CMS Collaboration), Searches for pair production of charginos and top squarks in final states with two oppositely charged leptons in proton-proton collisions at $\sqrt{s} = 13$ TeV, J. High Energy Phys. 11 (2018) 079.
[133] M. Aaboud *et al.* (ATLAS Collaboration), Search for photonic signatures of gauge-mediated supersymmetry in 13 TeV pp collisions with the ATLAS detector, Phys. Rev. D **97**, 092006 (2018).
[134] G. Aad *et al.* (ATLAS Collaboration), Search for supersymmetry in events with four or more charged leptons in 139 fb^{-1} of $\sqrt{s} = 13$ TeV pp collisions with the ATLAS detector, J. High Energy Phys. 07 (2021) 167.
[135] M. Aaboud *et al.* (ATLAS Collaboration), Search for electroweak production of supersymmetric states in scenarios with compressed mass spectra at $\sqrt{s} = 13$ TeV with the ATLAS detector, Phys. Rev. D **97**, 052010 (2018).

[136] A. M. Sirunyan *et al.* (CMS Collaboration), Search for new physics in events with two soft oppositely charged leptons and missing transverse momentum in proton-proton collisions at $\sqrt{s} = 13$ TeV, Phys. Lett. B **782**, 440 (2018).
[137] A. M. Sirunyan *et al.* (CMS Collaboration), Search for supersymmetric partners of electrons and muons in proton-proton collisions at $\sqrt{s} = 13$ TeV, Phys. Lett. B **790**, 140 (2019).
[138] F. Staub, SARAH, arXiv:0806.0538.
[139] F. Staub, SARAH 3.2: Dirac Gauginos, UFO output, and more, Comput. Phys. Commun. **184**, 1792 (2013).
[140] F. Staub, SARAH 4: A tool for (not only SUSY) model builders, Comput. Phys. Commun. **185**, 1773 (2014).
[141] F. Staub, Exploring new models in all detail with SARAH, Adv. High Energy Phys. **2015**, 840780 (2015).
[142] W. Porod, SPheno, a program for calculating supersymmetric spectra, SUSY particle decays and SUSY particle production at $e+$ $e-$ colliders, Comput. Phys. Commun. **153**, 275 (2003).
[143] W. Porod and F. Staub, SPheno 3.1: Extensions including flavour, *CP*-phases and models beyond the MSSM, Comput. Phys. Commun. **183**, 2458 (2012).
[144] W. Porod, F. Staub, and A. Vicente, A flavor Kit for BSM models, Eur. Phys. J. C **74**, 2992 (2014).
[145] G. Belanger, F. Boudjema, A. Pukhov, and A. Semenov, MicrOMEGAs: A Program for calculating the relic density in the MSSM, Comput. Phys. Commun. **149**, 103 (2002).
[146] G. Belanger, F. Boudjema, C. Hugonie, A. Pukhov, and A. Semenov, Relic density of dark matter in the NMSSM, J. Cosmol. Astropart. Phys. 09 (2005) 001.
[147] G. Belanger, F. Boudjema, A. Pukhov, and A. Semenov, MicrOMEGAs 2.0: A Program to calculate the relic density of dark matter in a generic model, Comput. Phys. Commun. **176**, 367 (2007).
[148] G. Belanger, F. Boudjema, A. Pukhov, and A. Semenov, MicrOMEGAs: A tool for dark matter studies, Nuovo Cimento C **033N2**, 111 (2010).
[149] G. Belanger, F. Boudjema, A. Pukhov, and A. Semenov, MicrOMEGAs_3: A program for calculating dark matter observables, Comput. Phys. Commun. **185**, 960 (2014).
[150] D. Barducci, G. Belanger, J. Bernon, F. Boudjema, J. Da Silva, S. Kraml, U. Laa, and A. Pukhov, Collider limits on new physics within MicrOMEGAs, Comput. Phys. Commun. **222**, 327 (2018).
[151] P. Bechtle, O. Brein, S. Heinemeyer, G. Weiglein, and K. E. Williams, HiggsBounds: Confronting arbitrary Higgs sectors with exclusion bounds from LEP and the tevatron, Comput. Phys. Commun. **181**, 138 (2010).
[152] P. Bechtle, O. Brein, S. Heinemeyer, G. Weiglein, and K. E. Williams, HiggsBounds 2.0.0: Confronting neutral and charged Higgs sector predictions with exclusion bounds from LEP and the tevatron, Comput. Phys. Commun. **182**, 2605 (2011).
[153] P. Bechtle, O. Brein, S. Heinemeyer, O. Stål, T. Stefaniak, G. Weiglein, and K. E. Williams, HiggsBounds-4: Improved tests of extended Higgs sectors against exclusion bounds from LEP, the tevatron and the LHC, Eur. Phys. J. C **74**, 2693 (2014).
[154] P. Bechtle, D. Dercks, S. Heinemeyer, T. Klingl, T. Stefaniak, G. Weiglein, and J. Wittbrodt, HiggsBounds-5: Testing Higgs sectors in the LHC 13 TeV era, Eur. Phys. J. C **80**, 1211 (2020).
[155] P. Bechtle, S. Heinemeyer, O. Stål, T. Stefaniak, and G. Weiglein, HiggsSignals: Confronting arbitrary Higgs sectors with measurements at the Tevatron and the LHC, Eur. Phys. J. C **74**, 2711 (2014).
[156] O. Stål and T. Stefaniak, Constraining extended Higgs sectors with HiggsSignals, Proc. Sci. EPS-HEP2013 (**2013**) 314.
[157] P. Bechtle, S. Heinemeyer, O. Stål, T. Stefaniak, and G. Weiglein, Probing the standard model with Higgs Signal rates from the tevatron, the LHC and a future ILC, J. High Energy Phys. 11 (2014) 039.
[158] P. Bechtle, S. Heinemeyer, T. Klingl, T. Stefaniak, G. Weiglein, and J. Wittbrodt, HiggsSignals-2: Probing new physics with precision Higgs measurements in the LHC 13 TeV era, Eur. Phys. J. C **81**, 145 (2021).
[159] F. Feroz, M. P. Hobson, and M. Bridges, MultiNest: An efficient and robust Bayesian inference tool for cosmology and particle physics, Mon. Not. R. Astron. Soc. **398**, 1601 (2009).
[160] E. Aprile *et al.* (XENON Collaboration), Constraining the spin-dependent WIMP-nucleon cross sections with XENON1T, Phys. Rev. Lett. **122**, 141301 (2019).
[161] M. Tanabashi, K. Hagiwara, Hikasa *et al.* (Particle Data Group Collaboration), Review of particle physics, Phys. Rev. D **98**, 030001 (2018).
[162] J. E. Camargo-Molina, B. O'Leary, W. Porod, and F. Staub, Vevacious: A tool for finding the global minima of one-loop effective potentials with many scalars, Eur. Phys. J. C **73**, 2588 (2013).
[163] J. E. Camargo-Molina, B. Garbrecht, B. O'Leary, W. Porod, and F. Staub, Constraining the natural MSSM through tunneling to color-breaking vacua at zero and non-zero temperature, Phys. Lett. B **737**, 156 (2014).
[164] W. Beenakker, R. Hopker, and M. Spira, PROSPINO: A Program for the production of supersymmetric particles in next-to-leading order QCD, arXiv:hep-ph/9611232.
[165] J. Alwall, M. Herquet, F. Maltoni, O. Mattelaer, and T. Stelzer, MadGraph 5: Going Beyond, J. High Energy Phys. 06 (2011) 128.
[166] E. Conte, B. Fuks, and G. Serret, MadAnalysis 5, A user-friendly framework for collider phenomenology, Comput. Phys. Commun. **184**, 222 (2013).
[167] T. Sjöstrand, S. Ask, J. R. Christiansen, R. Corke, N. Desai, P. Ilten, S. Mrenna, S. Prestel, C. O. Rasmussen, and P. Z. Skands, An introduction to PYTHIA 8.2, Comput. Phys. Commun. **191**, 159 (2015).
[168] M. Drees, H. Dreiner, D. Schmeier, J. Tattersall, and J. S. Kim, CheckMATE: Confronting your favourite new physics model with LHC data, Comput. Phys. Commun. **187**, 227 (2015).
[169] D. Dercks, N. Desai, J. S. Kim, K. Rolbiecki, J. Tattersall, and T. Weber, CheckMATE 2: From the model to the limit, Comput. Phys. Commun. **221**, 383 (2017).
[170] J. S. Kim, D. Schmeier, J. Tattersall, and K. Rolbiecki, A framework to create customised LHC analyses within CheckMATE, Comput. Phys. Commun. **196**, 535 (2015).

[171] J. de Favereau, C. Delaere, P. Demin, A. Giammanco, V. Lemaître, A. Mertens, and M. Selvaggi (DELPHES 3 Collaboration), DELPHES 3, A modular framework for fast simulation of a generic collider experiment, J. High Energy Phys. 02 (2014) 057.

[172] G. Alguero, J. Heisig, C. K. Khosa, S. Kraml, S. Kulkarni, A. Lessa, H. Reyes-González, W. Waltenberger, and A. Wongel, Constraining new physics with SModelS version 2, J. High Energy Phys. 08 (2022) 068.

[173] K. J. de Vries *et al.*, The pMSSM10 after LHC Run 1, Eur. Phys. J. C **75**, 422 (2015).

[174] J. C. Costa *et al.*, Likelihood analysis of the Sub-GUT MSSM in light of LHC 13-TeV data, Eur. Phys. J. C **78**, 158 (2018).

[175] P. Cox, C. Han, and T. T. Yanagida, Muon g-2 and coannihilating dark matter in the minimal supersymmetric standard model, Phys. Rev. D **104**, 075035 (2021).

[176] W. Altmannshofer and D. M. Straub, Viability of MSSM scenarios at very large $\tan\beta$, J. High Energy Phys. 09 (2010) 078.

[177] B. Fuks, M. Klasen, D. R. Lamprea, and M. Rothering, Gaugino production in proton-proton collisions at a center-of-mass energy of 8 TeV, J. High Energy Phys. 10 (2012) 081.

[178] B. Fuks, M. Klasen, D. R. Lamprea, and M. Rothering, Precision predictions for electroweak superpartner production at hadron colliders with RESUMMINO, Eur. Phys. J. C **73**, 2480 (2013).

[179] J. Cao, Y. He, L. Shang, Y. Zhang, and P. Zhu, Current status of a natural NMSSM in light of LHC 13 TeV data and XENON-1T results, Phys. Rev. D **99**, 075020 (2019).

[180] G. Aad *et al.* (ATLAS Collaboration), Search for charginos and neutralinos in final states with two boosted hadronically decaying bosons and missing transverse momentum in pp collisions at $\sqrt{s} = 13$ TeV with the ATLAS detector, Phys. Rev. D **104**, 112010 (2021).

[181] M. Chakraborti, S. Heinemeyer, and I. Saha, Improved $(g\text{-}2)_\mu$ Measurements and Supersymmetry: Implications for e^+e^- colliders, in *International Workshop on Future Linear Colliders* (2021), 5, arXiv:2105.06408.

[182] ILC Collaboration, The International Linear Collider Technical Design Report—Volume 2: Physics, arXiv:1306.6352.

[183] H. Abramowicz *et al.* (CLIC Detector, Physics Study Collaborations), Physics at the CLIC $e+e-$ Linear Collider—Input to the Snowmass process 2013, in Community Summer Study 2013: Snowmass on the Mississippi (2013), 7, arXiv:1307.5288.

[184] T. K. Charles *et al.* (CLICdp, CLIC Collaborations), The Compact Linear Collider (CLIC)—2018 Summary Report, arXiv:1812.06018.

[185] D. P. Aguillard *et al.* (Muon g-2 Collaboration), Measurement of the positive muon anomalous magnetic moment to 0.20 ppm, Phys. Rev. Lett. **131**, 161802 (2023).